Journal of Membrane Science 622 (2021) 118931

Contents lists available at ScienceDirect

Journal of Membrane Science

journal homepage: http://www.elsevier.com/locate/memsci

Computational fluid dynamics simulations of unsteady mixing in spacer-filled direct contact membrane distillation channels

Jincheng Lou [a], Jacob Johnston [a], Tzahi Y. Cath [b], Denis Martinand [c], Nils Tilton [a,*]

[a] Mechanical Engineering, Colorado School of Mines, United States
[b] Civil and Environmental Engineering, Colorado School of Mines, United States
[c] Aix-Marseille Univ, CNRS, Centrale Marseille, M2P2, Marseille, France

ARTICLE INFO

Keywords:
Membrane distillation
Temperature polarization
Concentration polarization
Immersed boundary method
Vortex shedding

ABSTRACT

Direct contact membrane distillation (DCMD) is a promising means of concentrating brines to their saturation limit. During that process, membrane spacers play a key role in temperature polarization, concentration polarization, and mineral scaling. These interactions are not well understood, because they are difficult to study experimentally and numerically, and the flow regimes are not fully charted. We consequently develop a tailored in-house CFD code that simulates unsteady two-dimensional heat and mass transport in plate-and-frame DCMD systems with cylindrical spacers. The code uses a combination of finite-volume methods in space, projection methods in time, and recent advances in immersed boundary methods for the spacer surfaces. Using the code, we explore how the transition to unsteady laminar vortex shedding affects polarization and permeate production of DCMD systems. We show that the impact of spacers can be explained by examining the various steady and unsteady vortical flow structures generated in the bulk and near the membranes. Overall, we show that though unsteady vortex structures tend to mix temperature polarization layers with the bulk, they are not similarly able to mix the concentration layers. Rather, vortical structures tend to create regions of preferential salt accumulation. In the vortex shedding regime, the net result is that spacers often increase vapor production at the expense of increasing the risk of mineral scaling.

1. Introduction

Membrane distillation is a promising means of concentrating brines to their saturation limit, after which they can be discharged to crystallizers or evaporation ponds [1–12]. The current study focuses on direct contact membrane distillation (DCMD), in which warm feed and cool distillate water flow on opposite sides of a hydrophobic microporous membrane in a co-current or counter-current manner, as sketched in Fig. 1. The hydrophobic membrane creates vapor-liquid interfaces on the feed and distillate sides of the membrane. The temperature difference across the membrane causes water to evaporate from the feed side of the membrane, travel through the vapor-filled pores, and condense on the distillate side of the membrane. Non-volatile solutes remain in the feed. Compared to reverse osmosis (RO), DCMD can treat hypersaline brines because it is comparatively insensitive to osmotic pressure and rejects 99–100% of salts. While RO can treat NaCl solutions to approximately 70 g/L, the limit for DCMD is approximately 300 g/L [13]. DCMD also operates at feed temperatures below 90 $^{\circ}C$ that are readily produced by renewable energy.

Temperature and concentration polarization are two crucial factors that affect DCMD treatment of hypersaline brines [2,14]. Temperature polarization is the reduction in the transmembrane temperature difference due to heat transfer through the membrane, as illustrated in Fig. 1. Concentration polarization is the accumulation of solutes adjacent to the feed side of the membrane. Both polarization phenomena reduce the transmembrane vapor flux by reducing the transmembrane partial vapor pressure difference. Concentration polarization also causes mineral scaling, which occurs when the concentration at the membrane surface exceeds the saturation limit of a solute. This blocks the membrane and can lead to pore wetting and permanent membrane damage.

Temperature and concentration polarization are further complicated by spacers, a mesh-like material that separates tightly packed membrane sheets, as illustrated in Fig. 2(*a*). Thinner spacers increase the membrane surface area in a system volume, but at the expense of increasing the channel pressure drop and pumping costs required to drive the feed and distillate flows. Spacers also create regions of preferential solute accumulation and precipitation. Though this is documented for RO [15–21], there is less work on scaling in DCMD systems. Literature suggests that

* Corresponding author.
E-mail address: ntilton@mines.edu (N. Tilton).

https://doi.org/10.1016/j.memsci.2020.118931
Received 16 July 2020; Received in revised form 22 November 2020; Accepted 25 November 2020
Available online 10 December 2020
0376-7388/© 2020 Elsevier B.V. All rights reserved.

Nomenclature

B	spacer blockage ratio
$\Delta P/L$	feed channel pressure drop (Pa/m)
ΔT_m	transmembrane temperature difference ($^{\circ}C$)
Δ	membrane thickness (m)
H	transmembrane thermal efficiency
$\widehat{y}_c$	spacer non-dimensional offset
Λ	latent heat of water (J/kg)
λ_{in}^d	distillate inlet latent heat of water (J/kg)
λ_{in}^f	feed inlet latent heat of water (J/kg)
u	velocity vector (m/s)
M	dynamic viscosity (Pa s)
N	kinematic viscosity (m^2/s)
Ω	vorticity s^{-1}
ρ	density (kg/m^3)
ρ^f, ρ^d	density of feed and distillate fluid (kg/m^3)
τ_m	shear stress on membrane (Pa)
CPC_{max}	maximum concentration polarization coefficient
$\widehat{\delta}_c$	non-dimensional concentration boundary layer thickness
$\widehat{\delta}_T$	non-dimensional thermal boundary layer thickness
a_w	water activity
B	vapor permeability (kg/m^2 s Pa)
b	NaCl molality (mol/kg)
c	concentration (g/L)
c_m	membrane surface concentration (g/L)
c_p	specific heat capacity (J/kg K)
C_{in}	feed concentration (g/L)
D	mass diffusivity (m^2/s)
D_{sp}	spacer diameter (m)
H	channel height (m)
j_v	transmembrane mass flux (kg/m^2 s)
k	fluid thermal conductivity (W/m $^{\circ}C$)
k_m	membrane thermal conductivity (W/m $^{\circ}C$)
L	channel length (m)
Le	Lewis number
p	pressure (Pa)
p_m^f, p_m^d	partial vapor pressure on the feed and distillate side of membrane (Pa)
P^{sat}	water vapor saturation pressure (Pa)
q_c	transmembrane conductive heat flux (W/m^2)
Re	Reynolds number
Re_c	critical Reynolds number
Re_f, Re_d	feed and distillate flow Reynolds number
St	Strouhal number
St_c	critical Strouhal number
T	temperature ($^{\circ}C$)
t	time (s)
T_m^f, T_m^d	membrane surface temperature on the feed and distillate side ($^{\circ}C$)
T_{in}^f, T_{in}^d	feed and distillate inlet temperature ($^{\circ}C$)
u, v	velocity component along x and y coordinates (m/s)
U_{in}	inlet velocity (m/s)
v_m	local transmembrane vapor flux (LMH)
v_m^{ave}	average transmembrane vapor flux (LMH)
x, y	Cartesian coordinates (m)
y_c	spacer vertical offset (m)
CPC	concentration polarization coefficient
LMH	Lm^{-2} hr^{-1}

solute accumulation tends to occur near "stagnant" or "dead" zones [22–26]. The definitions of "stagnant" or "dead" are not always precise, but they tend to refer to locations on the membrane where mixing is weak [23,24,26–28]. These often form near contact points where spacers meet the membrane [23,24,27]. Fig. 2(*b*) shows a membrane that experienced scaling in a RO system operated by Desalitech. An autopsy indeed suggested that scaling occurred near contact points (personal communication).

There is potential to increase the water recovery, energy efficiency, and membrane life of DCMD systems by designing spacers that strike a balance between maximizing membrane packing while minimizing the downstream pressure drop, polarization, and scaling. Designing such spacers is complicated by the coupled heat and mass transport in the feed, membrane, and distillate. These coupled processes are not fully understood, particularly in the presence of spacers. Because these processes are difficult to observe experimentally [25,29,30], computational fluid dynamics (CFD) offers a valuable complement that predicts the full temperature, concentration, and velocity fields [31–58].

CFD studies have made important contributions to understanding the effects of spacers on transport in membrane processes, as reviewed in Ref. [59–62]. Our own review finds three persistent challenges. The first is the simulation of near-membrane transport, which is difficult even in the absence of spacers. For pressure-driven processes such as RO, the dependence of the transmembrane flow on the pressure field causes traditional CFD methods to lose accuracy [63]. For DCMD, the accurate prediction of polarization requires the simultaneous simulation of the coupled feed channel, membrane, and distillate channel flows [14]. Due in part to these complications, studies of spacers sometimes neglect the membrane altogether [64–78]. Such studies focus on the effects of spacers on the downstream pressure drop and near-membrane shear stress.

A second challenge arises because the flow regime in spacer-filled channels is not fully understood. Though spacers are often called "turbulence promoters," it is not clear whether membrane systems operate in turbulent regimes. RO and DCMD systems typically operate with Reynolds numbers in the range $Re \leq 1000$, where $Re = U_{in}H/\nu$ is defined

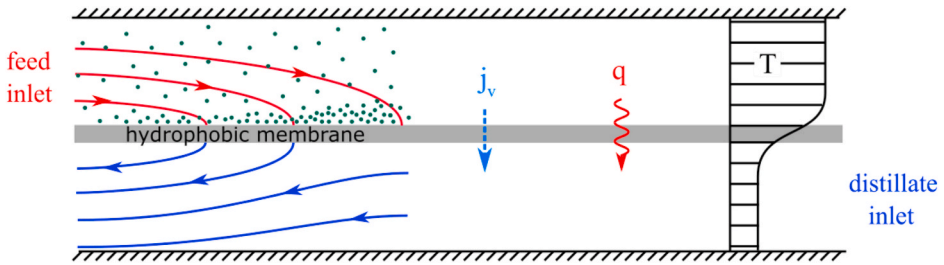

Fig. 1. Sketch (not to scale) that demonstrates concentration and temperature polarization in a counter-current DCMD system. Concentration polarization is shown by the solid dots.

using the mean feed inlet velocity U_{in} and feed channel height H (see Fig. 3). In this range, experiments [42,62,78–80] and simulations [42,43,62,73–87] suggest the flow is steady at low Re, and transitions to unsteady laminar vortex shedding at higher Re. The critical Reynolds number Re_c for transition varies between roughly $70 \leq Re_c \leq 500$, depending on the spacer geometry [42,62,73,75,76,78,79,84–86]. Studies suggest that vortex shedding reduces polarization and scaling by increasing shear stress near the membrane and directing bulk fluid towards the membrane [42,81–85]. Comparatively little work exists on the transition to turbulence [43,71,72,78].

A third challenge arises because CFD studies typically simulate spacers using body-fitted grids. Such grids are time-consuming to generate and limit the number of simulations that can be reasonably performed. A similar situation is faced in simulations of porous media [88,89]. In that case, the state-of-the-art uses Immersed Boundary Methods (IBM) [90] that use a simple Cartesian grid, with grid points located in both the fluid and solid regions. Solid surfaces are modeled by introducing a body force in the governing equations to force the fluid velocity to zero in the solid. Depending on the implementation, this achieves the same order-of-accuracy as body-fitted grids.

The current study investigates how transition from steady flow to unsteady laminar vortex shedding affects polarization in DCMD systems. For that purpose, we develop a 2-D CFD code that solves the Navier-Stokes, continuity, advection-diffusion, and heat equations using a finite-volume method in space and an efficient projection method in time, as detailed in Ref. [91]. To investigate the influence of vortex shedding, we consider 2-D spacer filaments, as illustrated in Fig. 3. The spacers are simulated using recent advances in IBM. Though spacers are inherently 3-D, we focus on idealized 2-D spacers because their hydrodynamic stability is much better understood in the fluid mechanics literature [92], and their simplicity allows us to perform a comprehensive parametric study and identify fundamental transport phenomena. Specifically, we systematically vary the Reynolds numbers, spacer diameter, and spacer position, and explore their impacts on the flow regime, vortical flow structures, polarization, and system performance. It is our philosophy that elucidating such phenomena is prerequisite to intelligently designing 3-D spacers. 2-D spacers are also more amenable to quantitative experimental study, which is the topic of ongoing work in our group. Considering the spacers encountered in literature [25], our geometry is closest to "ladder-type" spacers [25,93,94].

The remainder of this study is organized as follows. Section 2 presents the system geometry, governing equations, and boundary conditions. Section 3 summarizes the numerical methods and code validation. Section 4 presents our results and discussion. Section 5 presents our conclusions.

2. Geometry and governing equations

We consider a plate-and-frame DCMD system with feed and distillate channels of length L and height H, as illustrated in Fig. 3. Both channels have an idealized cylindrical spacer of diameter D_{sp}, centered at $x = L/2$ and a distance y_c from the membrane. NaCl solution enters the feed channel with temperature T_{in}^f, concentration C_{in}, and mean velocity U_{in}. Pure water enters the distillate channel with temperature T_{in}^d and mean velocity U_{in}. We focus on counter-current operation because it is preferred in the literature. Though Fig. 3 shows the membrane as a shaded region about $y = 0$, we model transmembrane heat and mass transport using effective interface conditions that couple the feed $(0 \leq y \leq H)$ and distillate $(-H \leq y \leq 0)$ channels. We set $H = 2$ mm, which is typical of DCMD systems. We set $L = 2$ cm, which was found to sufficiently minimize the impact of outlet conditions on upstream flow. Though our geometry mimics typical lab-scale DCMD systems, future industrial systems might replace the feed plate with a second membrane. For the current scope, we limit ourselves to one membrane for several reasons. First, it facilitates comparison with lab-scale measurements. Next, adding a second membrane requires the simulation of an additional distillate channel and spacer. The resulting simulation of three coupled channels and spacers becomes computationally expensive, making parametric study prohibitive. Finally, our objective is to understand how spacers impact transition to vortex shedding, and how this transition impacts polarization. Results shown in Table 1 of section 3.1 show that the membrane has a negligible impact on the flow regime and vortical flow structures. Rather, these are primarily determined by the spacer position and diameter.

2.1. Transmembrane heat and mass transport

We model heat and mass transport through the membrane as previously described in Lou et al. [14]. We only highlight the key features here. As in most previous literature, we assume that the transmembrane mass flux, j_v, is linearly proportional to the transmembrane vapor pressure difference [95],

$$j_v = -B\left(p_m^f - p_m^d\right), \tag{1}$$

where B is the vapor permeability and p_m^f and p_m^d are the local partial vapor pressures on the feed and distillate membrane surfaces, respectively. Note that j_v is negative when the transmembrane vapor flux flows from the feed into the distillate. These pressures are functions of the local temperature and concentration at the membrane surface [96], and are evaluated as the product of the saturation pressure P^{sat} and water activity a_w,

$$p_m = a_w P^{sat}, \quad P^{sat} = \exp\left(23.238 - \frac{3841}{T_m + 228.15}\right), \tag{2}$$

where P^{sat} is determined using the Antoine equation [97], and T_m is the local temperature on the membrane surface. The activity is determined from the expression $a_w = 1 - 0.03112b - 0.001482b^2$ [60], where b is the NaCl molality (mol/kg). This expression is valid from zero salinity to saturation [60]. We assume complete salt rejection, such that $a_w = 1$ in the distillate.

As in most previous literature, we model transmembrane heat conduction as

$$q_c = -\frac{k_m}{\delta}\left(T_m^f - T_m^d\right), \tag{3}$$

where δ and k_m are the membrane thickness and thermal conductivity, respectively, and T_m^f and T_m^d are the temperatures on the feed and

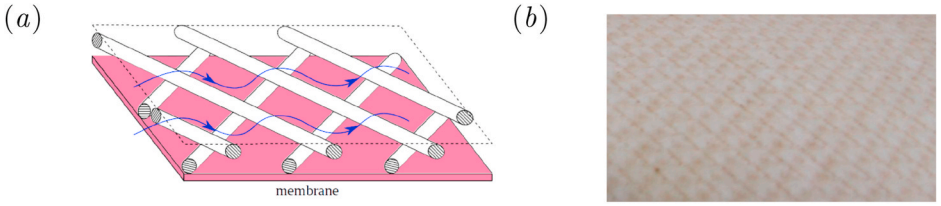

Fig. 2. (*a*) Sketch (not to scale) of a membrane spacer. (*b*) Photographic image, courtesy of Desalitech, of mineral scaling (brown regions) on a reverse osmosis membrane. (For interpretation of the references to color in this figure legend, the reader is referred to the Web version of this article.)

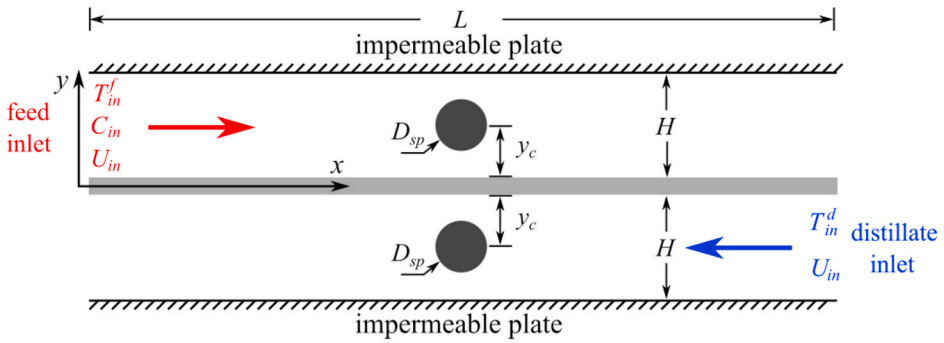

Fig. 3. Sketch (not to scale) of the 2-D DCMD flow channels considered in this study. Each channel has a length L and height H. The membrane is shaded gray. Both channels have a cylindrical spacer filament centered at $x = L/2$ and $y = \pm y_c$. NaCl solution enters the feed channel with temperature T_{in}^f, concentration C_{in}, and mean velocity U_{in}. Pure water enters the distillate channel with temperature T_{in}^d and mean velocity U_{in}.

Table 1
For the blockage ratios shown in column 1, columns 2 and 3 show our computed critical Reynolds numbers Re_c and Strouhal numbers St_c for the feed channel of a DCMD system with $\widehat{y}_c = 0.5$, $T_{in}^f = 80\,^{\circ}C$, $T_{in}^d = 20\,^{\circ}C$ and $C_{in} = 100$ g/L. Columns 4 and 5 show the corresponding predictions of Sahin and Owens [100] for a cylinder in a channel with two impermeable walls.

	DCMD system		Sahin and Owens	
β	Re_c	St_c	Re_c	St_c
0.3	213.0 ± 1.0	1.0429 ± 0.01	209.78	1.0465
0.5	166.0 ± 1.0	1.0193 ± 0.01	165.00	1.0197
0.7	106.0 ± 1.0	1.0076 ± 0.01	104.80	1.0204

distillate membrane surfaces, respectively. Note again that q_c is negative when heat is conducted from the feed channel into the distillate. Conservation of energy for liquid-vapor interfaces with phase change (see Leal [98]) requires that on the membrane feed surface, conductive heat transport within the liquid phase must equal

$$-k\frac{\partial T_m^f}{\partial y}\bigg|_{y=0^+} = j_v\lambda - \frac{k_m}{\delta}\left(T_m^f - T_m^d\right), \tag{4}$$

where λ is the latent heat per unit mass, and the "+" superscript signifies that the derivative is evaluated from the feed side of the membrane. We set $\lambda = (\lambda_{in}^f + \lambda_{in}^d)/2$, where λ_{in}^f and λ_{in}^d are evaluated using the feed and distillate conditions, respectively. Similar conditions are applied on the distillate surface. Finally, total salt rejection requires the summation of advective and conductive salt flux on the feed side of the membrane to be zero,

$$\frac{j_v c_m}{\rho} - D\frac{\partial c}{\partial y}|_{y=0^+} = 0, \tag{5}$$

where c_m is the salt concentration on the feed side of the membrane, and D is the effective mass diffusivity.

Consistent with much MD literature, we approximate the vapor permeability B as a constant membrane property, and the ratio k_m/δ as an effective heat transfer coefficient. Hereinafter, we set these to $B = 1.87\times 10^{-6}$ kg/m^2 s Pa and $k_m/\delta = 576.72$ W/m^2 K. These were determined experimentally in Lou et al. [14] for a 0.2 μm pore size polypropylene 3 M membrane.

2.2. Transport in the feed and distillate channels

The channel flows are governed by the incompressible continuity and Navier-Stokes equations for Newtonian fluids,

$$\nabla\cdot\mathbf{u} = 0, \tag{6}$$

$$\rho\left[\frac{\partial\mathbf{u}}{\partial t} + (\mathbf{u}\cdot\nabla)\mathbf{u}\right] = -\nabla p + \mu\nabla^2\mathbf{u}, \tag{7}$$

where $\mathbf{u} = [u\ v]$, p, ρ and μ are the fluid velocity vector, pressure, density, and dynamic viscosity, respectively. Within each channel, we neglect variations in density with temperature and concentration, because the maximum variation of density is typically within 3%. In each channel, we set the density to the inlet value. Heat and solute transport in the flow channels are governed by the thermal energy and advection-diffusion equation,

$$\rho c_p\left[\frac{\partial T}{\partial t} + (\mathbf{u}\cdot\nabla)T\right] = k\nabla^2 T, \tag{8}$$

$$\frac{\partial c}{\partial t} + (\mathbf{u}\cdot\nabla)c = D\nabla^2 c, \tag{9}$$

where c_p is the fluid heat capacity [99]. Appendix A.1 shows that the variation of thermo-physical properties with temperature and concentration has only a small impact (approximately 4% or less) for the systems considered in the current study. We consequently neglect these variations, because including them substantially increases the computational time. In each channel, we set the thermo-physical properties to those evaluated at the inlet conditions.

At the plates ($y = \pm H$) and spacer surfaces, we apply the no-slip, no-penetration, and no-flux conditions,

$$u = v = \nabla c\cdot\mathbf{n} = \nabla T\cdot\mathbf{n} = 0, \tag{10}$$

where $\mathbf{n}$ is the normal vector. The boundary conditions approximate the spacers as insulated, which is common in prior literature [42,62,80]. Conjugate heat transport between the spacers and fluids is left to future study, due in part to its formidable numerical challenges. On the membrane surfaces, we apply the no-slip condition, $u = 0$, and the following conditions determined from the models discussed in section 2.1. The feed side conditions are,

$$v = \frac{j_v}{\rho^f}, \quad -k\frac{\partial T}{\partial y}|_{y=0^+} + \frac{k_m}{\delta}T_m^f = j_v\lambda + \frac{k_m}{\delta}T_m^d, \quad vc_m - D\frac{\partial c}{\partial y}|_{y=0^+} = 0, \tag{11}$$

and the distillate side conditions are,

$$v = \frac{j_v}{\rho^d}, \quad -k\frac{\partial T}{\partial y}|_{y=0^-} - \frac{k_m}{\delta}T_m^d = j_v\lambda - \frac{k_m}{\delta}T_m^f. \tag{12}$$

At the channel inlets, we apply uniform temperature and concentration, and fully developed laminar velocity profiles with desired mean velocity U_{in},

$$u = 6U_{in}\left[\frac{y}{H} - \frac{y^2}{H^2}\right], \quad v = 0, \quad T = T_{in}, \quad c = C_{in}. \tag{13}$$

For all cases, the feed and distillate channels have identical mean inlet velocities, U_{in}. At the outlets, we apply the convective conditions $\partial g/\partial t + U_{in}(\partial g/\partial x) = 0$, where $g = [\mathbf{u}, T, c]$, as detailed in Ref. [91].

3. Methodology

We solve Eqns. (6)–(9) using the numerical methods described and validated in Lou et al. [14,91]. Further details and benchmarking are provided in appendix A. We set the initial flow fields to the inlet conditions, and integrate in time until the fields reach a steady-state or transition to vortex shedding. In the latter case, the simulation is run sufficiently long to minimize transient effects from the initial start-up.

3.1. Measure of critical Reynolds number and Strouhal number

Transition to vortex shedding depends on the size and location of the spacer filaments. For that purpose, we define the blockage ratio $\beta = D_{sp}/H$ and non-dimensional offset $\hat{y}_c = y_c/H$. We define the Reynolds number $Re = U_{in}H/\nu$, where ν is the kinematic viscosity. The feed and distillate channels have different Reynolds numbers, because ν in each channel is evaluated using the channel's inlet temperature and concentration. To compute the critical Reynolds numbers Re_c for transition to vortex shedding, we perform simulations to determine a pair of Reynolds numbers Re_1 and Re_2, for which $Re_2 - Re_1 \leq 2$, and for which the flow is steady at Re_1 and unsteady at Re_2. We then set $Re_c = (Re_1 + Re_2)/2$. For cases with vortex shedding, we compute the shedding frequency by measuring $\mathbf{u}$ in time at $x = 3L/5$ and $y = H/2$ (downstream of the feed spacer). We then perform a Fourier transform to extract the dominant frequency f, and define the Strouhal number $St = fH/U_{in}$.

Our code was previously validated without spacers in Ref. [14]. We validate our simulation of spacers by comparing with a theoretical analysis performed by Sahin and Owens [100] of vortex shedding over a cylinder placed on the centerline of a channel with two impermeable walls. Table 1 summarizes our computed Re_c and St_c for the feed channel of a DCMD system with blockage ratios $\beta = 0.3$, 0.5, and 0.7. The spacers are placed in the middle of the channels ($\hat{y}_c = 0.5$). Columns 2 and 3 present the results for the DCMD system when we set the operating temperatures and concentration to $T_{in}^f = 80\ ^\circ C$, $T_{in}^d = 20\ ^\circ C$, and $C_{in} = 100$ g/L, respectively. Columns 4 and 5 show there is excellent agreement with the theoretical predictions of Sahin and Owens [100]. We conclude that the membrane-normal velocity component has a negligible effect on transition to vortex shedding for the cases in Table 1.

3.2. System performance criteria

We investigate the system-level performance of DCMD systems by computing the transmembrane thermal efficiency [101],

$$\eta = \frac{q_v^{net}}{q_v^{net} + q_c^{net}} = \frac{\int_0^L j_v \lambda dx}{\int_0^L j_v \lambda dx + \int_0^L \frac{k_m}{\delta}\left(T_m^f - T_m^d\right)dx}, \tag{14}$$

where q_v^{net} is the net latent heat flux, and q_c^{net} is the net conductive heat flux. The definition of η quantifies the fraction of total heat transport across the membrane that contributes to water evaporation. We compute the pressure drop in the feed channel as,

$$\Delta P \Big/ L = \frac{P_{in} - P_{out}}{L}, \tag{15}$$

where P_{in} and P_{out} are the area-averaged feed pressures at the channel inlet and outlet. In the vortex shedding regime, we average $\Delta P/L$ in time. We characterize concentration polarization using a concentration polarization coefficient,

$$\mathrm{CPC}(x) = \frac{c_m(x)}{C_{in}}, \tag{16}$$

which is often used in previous literature [2,30,58,102–104]. Note that CPC = 1 denotes no concentration polarization, and CPC≫1 indicates strong polarization. We report the maximum CPC, denoted as CPC_{max}. This is motivated by DCMD's applications to treating high-concentration brines. In such applications, it is important to minimize CPC_{max} to avoid mineral scaling.

4. Results and discussion

We investigate the effects of spacers on flow regime and polarization by performing a parametric study in which we fix the operating temperatures $T_{in}^f = 80\ ^\circ C$, $T_{in}^d = 20\ ^\circ C$, and feed concentration $C_{in} = 100$ g/L, which are realistic conditions for DCMD. In the following sections, we systematically vary U_{in}, D_{sp}, and y_c to investigate the effects of the Reynolds number and spacer geometry.

4.1. Influence of Reynolds number

We investigate the effects of the Reynolds number by considering spacers on the channel centerline ($\hat{y}_c = 0.5$), blocking 50% of the channel ($\beta = 0.5$). We then vary the inlet velocity between $1.06 \times 10^{-2} < U_{in} < 6.34 \times 10^{-2}$ m/s. This varies the feed and distillate Reynolds numbers between $50 < Re_f < 300$ and $42 < Re_d < 126$. To demonstrate the impact on the flow regime, the left column of Fig. 4 shows instantaneous streamlines downstream of the feed spacer for $Re_f = 150$ (*a*) and 300 (*c*), respectively. The axes are non-dimensionalized as x/H and y/H. The right column shows the corresponding vorticity fields $\Omega = \partial v/\partial x - \partial u/\partial y$. Panels (*a*) and (*b*) show a steady regime with counter-rotating vortices in the cylinder wake. Panels (*c*) and (*d*) show that for supercritical Reynolds numbers ($Re > Re_c$), the flows exhibit two types of unsteady vortical structures. First, vortices in the wake are periodically shed from the cylinder and advected downstream in the bulk. This generates a procession of staggered vortex structures, akin to the von Kármán vortex street. These structures are clearly observable in the vorticity fields. Second, vortical structures with closed streamlines periodically form and travel downstream along the outer plate and membrane surface. These structures are clearly observable in the streamlines. The strength and number of these vortices increase with Reynolds number. We refer to the vortices on the outer plates as "plate-vortices," and those on the membrane as "membrane-vortices".

Fig. 5 shows our results for a full DCMD system operated at $U_{in} = 2.11 \times 10^{-2}$ m/s, for which $Re_f = 100$ and $Re_d = 42$. The streamlines in panel (*a*) show that both the feed and distillate channels are steady. The wake is larger in the feed channel, because the feed Reynolds number is larger than that in the distillate. Panel (*b*) shows the temperature field. We use different color scales for the feed and distillate channels to highlight cooling of the feed and heating of the distillate. Focusing on the feed channel, we observe that the fluid temperature remains constant, except in a thermal boundary layer adjacent to the membrane. The thermal boundary layer thickness grows with downstream distance, until it approaches the spacer. Panel (*a*) shows that the upstream cylinder surface decreases the cross-sectional flow area, accelerates the feed, and redirects warm fluid from the channel center toward the membrane. This decreases the boundary layer thickness as feed flows around the cylinder, after which the boundary layer relaxes and continues growing downstream. Similar behavior is observed in the distillate channel. Overall, the thermal layers are relatively thick, covering nearly 50% of the channel widths at the outlets.

Fig. 5 (*c*) shows the concentration field near the membrane, $0 < y/H < 0.2$. The concentration of the feed channel is constant, except in a thin boundary layer on the membrane. This layer is much thinner

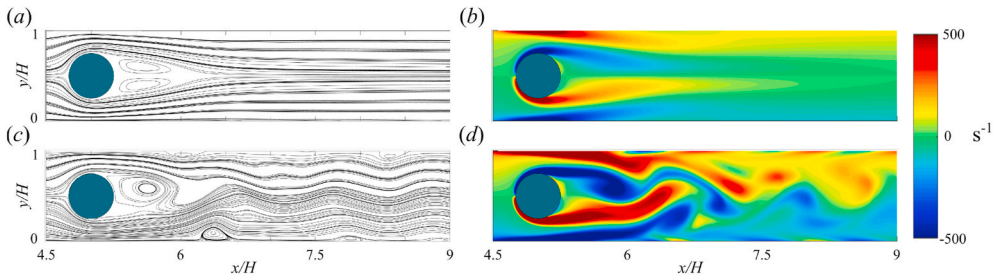

Fig. 4. Streamlines (left column) and vorticity field (right column) downstream of the feed spacer for $Re_f = 150$ (*a* and *b*) and 300 (*c* and *d*), when $\beta = 0.5$ and $\hat{y}_c = 0.5$.

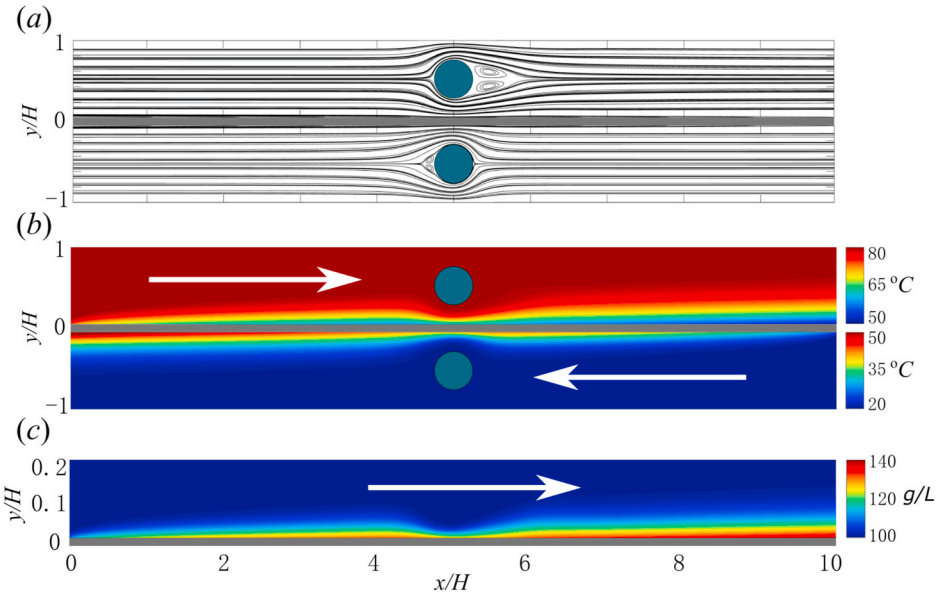

Fig. 5. Results when $Re_f = 100$. (*a*) Streamlines. (*b*) Temperature field. Different color scales are used in the distillate and feed channels. (*c*) Feed concentration field for $0 < y/H < 0.2$. The white arrows in panels (*b*) and (*c*) indicate the flow directions. (For interpretation of the references to color in this figure legend, the reader is referred to the Web version of this article.)

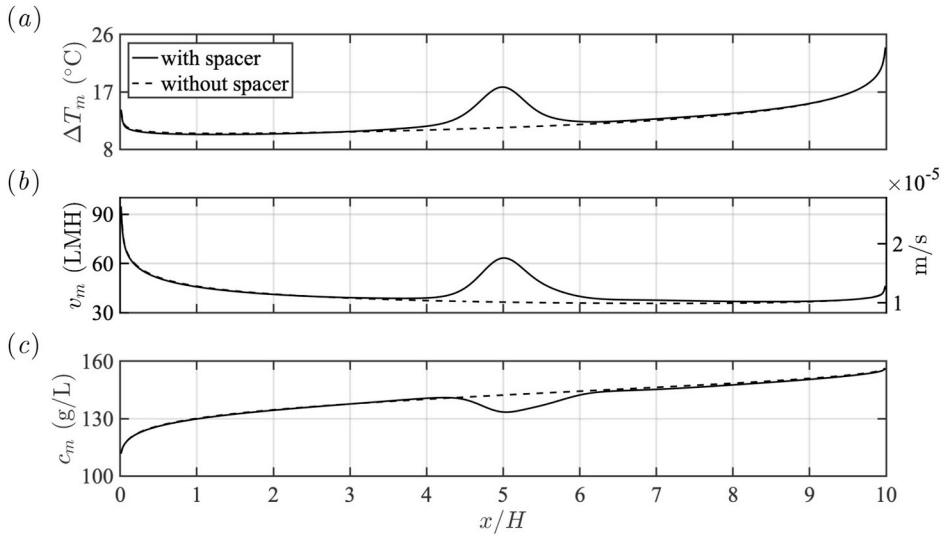

Fig. 6. Solid lines show (*a*) the transmembrane temperature difference ΔT_m, (*b*) the transmembrane vapor flux v_m, and (*c*) the membrane surface concentration c_m for the simulation shown in Fig. 5. Dashed lines show corresponding results for a simulation without spacers. The transmembrane vapor flux in panel (*b*) is shown in units of both LMH ($Lm^{-2}hr^{-1}$) and m/s.

than the thermal layer because the feed Lewis number is $Le = \alpha/D = 42$. As observed for the thermal layer, the concentration layer grows with downstream distance, except in a region near the upstream half of the cylinder, where the cylinder redirects lower-concentration bulk flow towards the membrane. Appendix B provides additional quantitative results for the boundary layer thicknesses.

The solid lines in Fig. 6 show the transmembrane temperature difference ΔT_m (*a*), transmembrane vapor flux v_m (*b*), and membrane surface concentration c_m (*c*) for the simulation shown in Fig. 5 ($Re_f = 100$). Note that we define $v_m = |j_v|/\rho_f$, i.e. the local transmembrane vapor flux is defined using the feed density, and is a positive quantity. The dashed lines show corresponding results without spacers. In a region roughly two diameters up and downstream from the cylinder center, redirection of the bulk flows towards the membrane increases ΔT_m. Panel (*b*) shows that this increases the local transmembrane vapor flux. Counterintuitively, panel (*c*) shows that the increase in v_m does not produce an increase in c_m. Rather, we see a decrease in c_m. This is because the reduced concentration boundary layer thickness (see appendix B) creates a steeper concentration gradient $\partial c/\partial y$ that increases solute diffusion away from the membrane. Outside the near-cylinder region, the cylinder has minimal impact. Overall, the spacers decrease temperature and concentration polarization, and produce an average transmembrane vapor flux of 43.9 LMH, compared to 39.6 LMH without spacers, an increase of 11.3%. Note that the short system length ($L = 2$ cm) produces higher average vapor flux values than typically observed in bench-scale systems. This is because longer systems have more heat exchange between the feed and distillate channels. The increased heat exchange decreases the average transmembrane temperature difference ΔT_m, and consequently the permeate flux [14].

Fig. 7 shows snapshots of the instantaneous streamlines (*a*), vorticity field (*b*), temperature field (*c*), and concentration field (*d*) when we increase the inlet velocity to $U_{in} = 6.34 \times 10^{-2}$ m/s, producing $Re_f = 300$ and $Re_d = 126$. The feed flow is now strongly supercritical, while the distillate flow remains steady. The streamlines show the presence of 3 membrane-vortices near $x/H = 6.5$, 8, and 9. Appendix C demonstrates the formation and evolution of these vortices. Panel (*b*) shows that in addition to the vorticity generated on the cylinder surface, considerable vorticity is generated on the plate and membrane around $x/H = 5$, where the cross-sectional flow area is minimized. Downstream from the cylinder, this vorticity separates from the plate and membrane, and interacts with the vortical structures in the bulk. Panel (*c*) shows that unsteady flow in the feed channel strongly mixes the thermal boundary layer with the bulk. However, panel (*d*) shows that the concentration layer is not similarly mixed, likely because it is much thinner than the thermal layer.

Closer inspection shows that the membrane-vortices play an important role in polarization. This is demonstrated in Fig. 8, which shows instantaneous streamlines superimposed on the temperature (panel *a*) and concentration (panels *b* and *c*) fields in the vicinity of the membrane-vortex nearest the cylinder. Panel (*a*) suggests that the leading edge of the vortex ejects cool fluid from near the membrane into the bulk. The concentration plots in panels (*b*) and (*c*) suggest that the vortex does not similarly eject high concentration fluid. Rather, panel (*c*) shows that the reverse flow beneath the vortex advects salt upstream, where it accumulates near the leading edge of the vortex. Indeed, we consistently find that solutes tend to accumulate near the leading edge of membrane-vortices.

The solid lines in Fig. 9 show ΔT_m (*a*), c_m (*b*), and v_m (*c*) for the simulation in Fig. 7. The dashed lines show corresponding results without spacers. Though the bulk flow is strongly unsteady, the results for ΔT_m, c_m, and v_m in Fig. 9 are all essentially steady, showing negligible variations in time. We offer a physical explanation for this behavior in appendix D. Specifically, we perform an order-of-magnitude analysis that suggests the dominant mechanisms for heat and salt transport near the membrane surface have much longer characteristic time-scales compared to the period of vortex shedding.

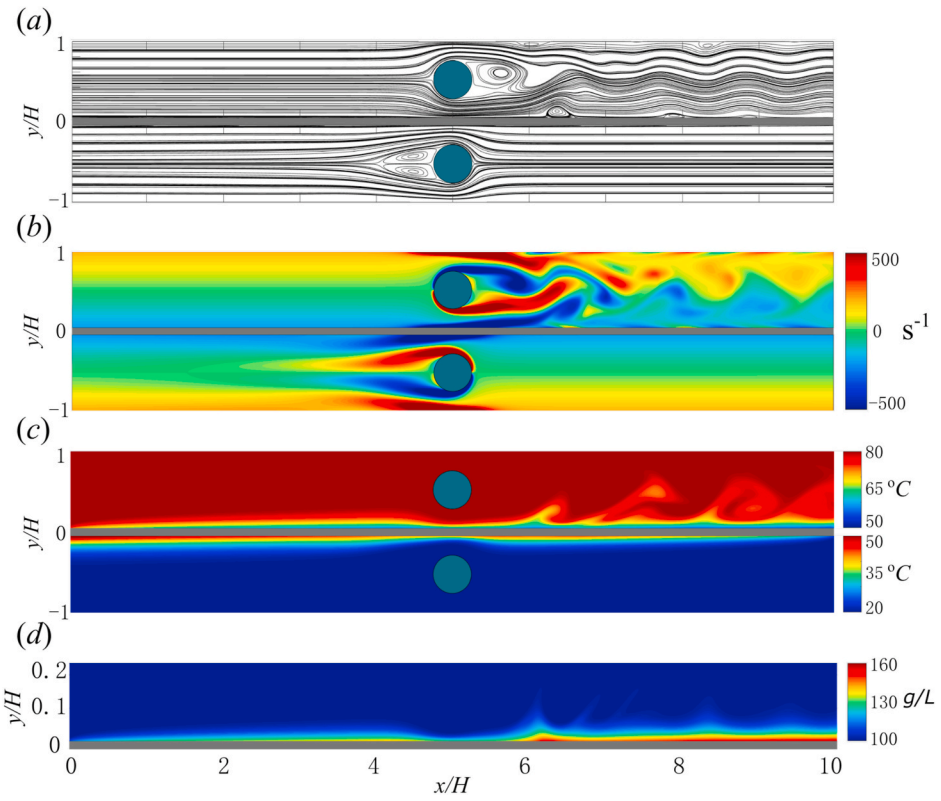

Fig. 7. Results when $Re_f = 300$. (*a*) Streamlines. (*b*) Vorticity field. (*c*) Temperature field, using different color scales in the distillate and feed channels. (*d*) Concentration field for $0 < y/H < 0.2$. (For interpretation of the references to color in this figure legend, the reader is referred to the Web version of this article.)

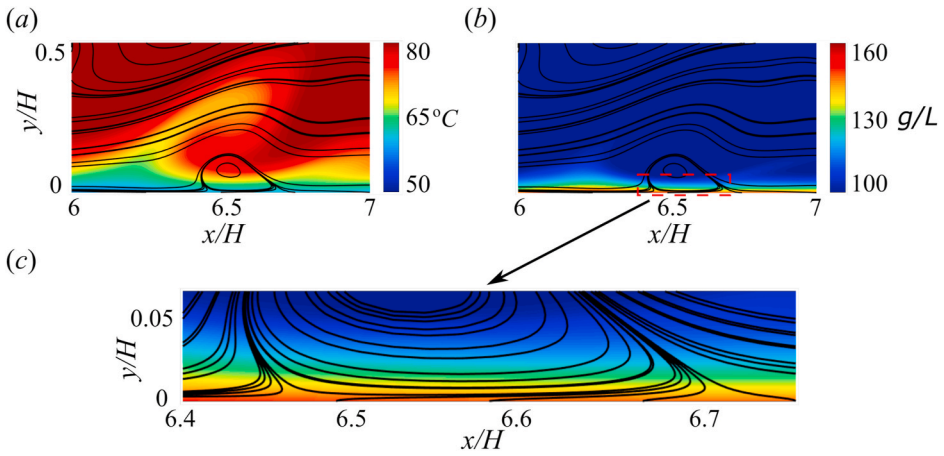

Fig. 8. Instantaneous streamlines superimposed on the temperature (panel *a*) and concentration (panel *b* and *c*) fields in the vicinity of the membrane-vortex nearest the cylinder.

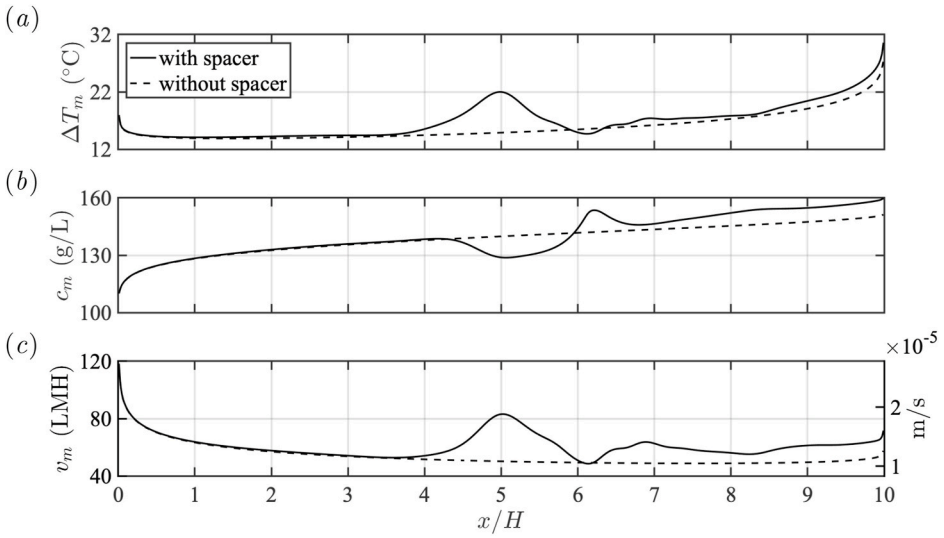

Fig. 9. The solid lines show (*a*) ΔT_m, (*b*) c_m, and (*c*) v_m for simulation in Fig. 7 ($Re_f = 300$), respectively. The dashed lines show corresponding results for a simulation without spacers.

Fig. 9(*a*) shows that the cylinder increases ΔT_m, not only near the cylinder, but also in the far downstream region. Fig. 9(*b*) shows that though c_m is reduced near the cylinder, it increases in the downstream region $x/H > 6$. The increase in c_m in the far-downstream region is likely due to the increased transmembrane flow v_m in that region. We also observe localized salt accumulation near $x/H = 6.2$, where c_m reaches a local maximum of 153 g/L. This is consistent with our discussion of Fig. 8 (*b*). Though literature often attributes mineral scaling to contact points between the spacer and membrane, our results show that spacers can create regions of salt accumulation without actually contacting the membrane. Moreover, the fluid structures causing salt accumulation are the same structures that effectively mix the temperature field. Overall, the simulation at $Re_f = 300$ produces an average transmembrane vapor flux of 63.0 LMH with spacers, compared to 54.0 LMH without, an increase of 16.5%.

The solid lines in Fig. 10 show the variation of the average vapor flux v_m^{ave} (*a*), thermal efficiency η (*b*), feed pressure drop $\Delta P/L$ (*c*), and maximum concentration polarization coefficient CPC_{max} (*d*) with Re_f. The dashed lines show corresponding results without spacers. The supercritical regime ($Re_f > Re_c$) is shaded gray. Panel (*a*) shows that simulations with spacers produce more vapor flux than those without, particularly at supercritical Reynolds numbers. At $Re_f = 300$, the system with spacers produces around 14% more vapor flux than without. In panel (*b*), the cases with spacers produce only slightly higher η than those without (an increase below 1%). This is because although spacers increase permeate production and transmembrane latent heat transfer, the decrease in temperature polarization also increases transmembrane conductive heat transfer. Panel (*c*) shows that spacers increase vapor production and thermal efficiency at the expense of much larger pressure drops. At $Re_f = 300$, the system with a spacer requires 4 times the pressure drop in a system without. In panel (*d*), we find that transition to vortex shedding causes a sudden increase in CPC_{max}. In the steady regime, CPC_{max} of the cases with spacers decreases with increasing Re_f, and is less than that observed in systems without spacers. This is explained by our discussion of Fig. 6(*b*). However, in the unsteady regime, CPC_{max} of the cases with spacers increases rapidly and shows higher values than cases without spacers. At $Re_f = 300$, the maximum concentration on the membrane surface is nearly 1.6 times the inlet feed value when the spacers are present.

Overall, Fig. 10 suggests that vortex shedding increases permeate production at the expense of increased concentration polarization. This trend persists throughout our study. This suggests that when treating low-concentration feeds, one can increase the feed flow rate to operate in a vortex shedding regime that increases vapor production. However,

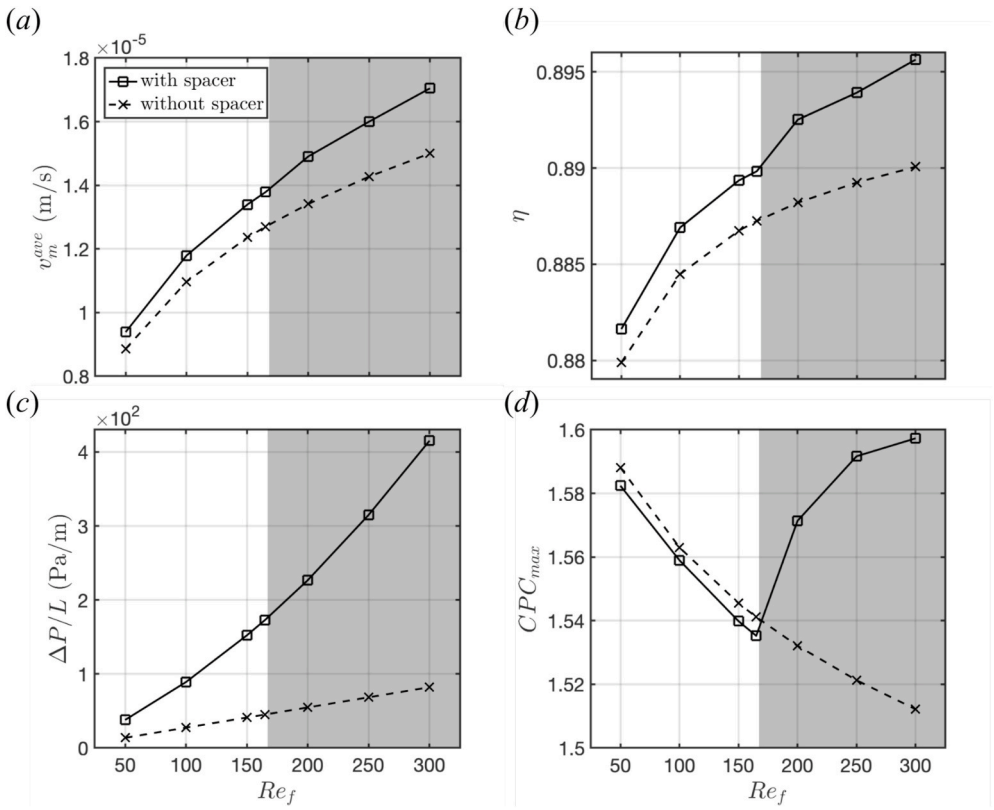

Fig. 10. Impact of the Reynolds number on system-level performance when $\beta = 0.5$ and $\hat{y}_c = 0.5$. The solid lines show the variation of the average vapor flux v_m^{ave} (*a*), thermal efficiency η (*b*), feed pressure drop $\Delta P/L$ (*c*), and maximum concentration polarization coefficient CPC_{max} (*d*) with Re_f. The dashed lines show corresponding results without spacers. The supercritical regime ($Re_f > Re_c$) is shaded gray in the plots.

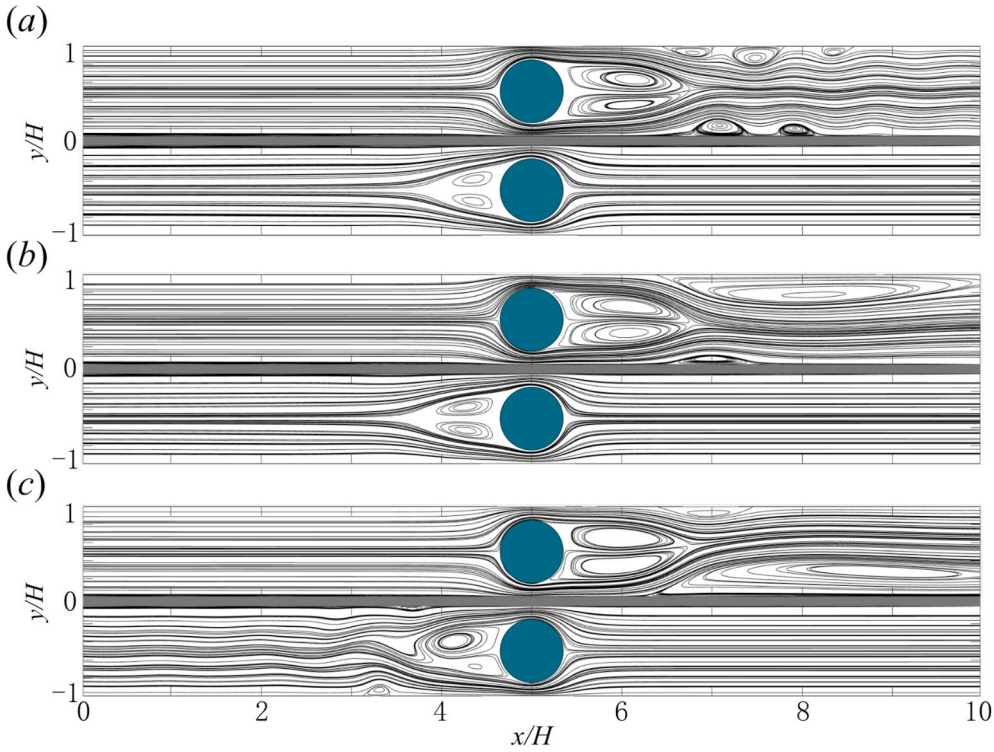

Fig. 11. Feed and distillate streamlines when $\beta = 0.7$, $\hat{y}_c = 0.5$, and $Re_f = 200$ (*a*), 240 (*b*), and 300 (*c*), respectively.

when treating high-concentration feeds, it is safer to operate at lower feed flow rates that produce steady flow regimes with reduced risk of precipitation. Naturally, these results are subject to our consideration of idealized 2D spacers. The key conclusion is that, in the unsteady regime, the same fluid structure responsible for decreasing temperature polarization can simultaneously increase concentration polarization and mineral scaling.

4.2. Influence of blockage ratio β

To investigate the blockage ratio, we repeated the analysis demonstrated in the previous section, but set $\beta = 0.3$ and 0.7. The spacers remain on the channel centerlines ($\hat{y}_c = 0.5$). Overall, we found that the small blockage ratio ($\beta = 0.3$) produced qualitatively similar results to those observed for $\beta = 0.5$, though the impact of small spacers on polarization and vapor production is less than that for $\beta = 0.5$. For brevity, these results are not presented.

In contrast to our results for $\beta = 0.3$, large blockage ratios produce markedly different results. Fig. 11(*a*) shows the feed and distillate channel streamlines at $Re_f = 200$ when $\beta = 0.7$. The feed flow has transitioned to vortex shedding, generating large membrane-vortices due to the sudden expansion downstream of the cylinder. Panel (*b*) shows that when Re_f is increased to 240, the feed flow transitions to a new steady regime characterized by a large plate-vortex and a small membrane-vortex. Panel (*c*) shows that when Re_f is further increased to 300, the asymmetry in the feed channel reverses, such that the membrane-vortex is much larger than the plate-vortex.

The steady asymmetric feed flows observed in Fig. 11(*b*) and (*c*) are examples of what are called "bi-stable states" in the fluid mechanics community [100]. To our knowledge, they have never previously been observed in membrane filtration systems. We repeated the simulations demonstrated in panels (*b*) and (*c*) with random initial conditions, and found that either state can be selected, such that the larger vortex appears on either the membrane or plate. This again shows that the small transmembrane velocity does not impact the flow regime from what is observed in channels with two impermeable plates.

Fig. 12(*a*) shows the temperature field when $\beta = 0.7$, $\hat{y}_c = 0.5$, and $Re_f = 300$. The large membrane-vortex causes the formation of a large region of cool fluid along much of the downstream membrane surface. This forms because the closed streamlines in the membrane-vortex only allow heat to be exchanged with the outside flow through diffusion normal to the streamlines. This diffusion is a slow process compared to heat advection within the vortices. Fig. 12(*b*) shows the downstream variation of c_m for $\beta = 0.7$, $\hat{y}_c = 0.5$ when $Re_f = 200$ (solid lines), 240 (dashed lines), and 300 (dash-dotted lines). All three supercritical states produce localized salt accumulation downstream of the feed spacer.

The solid lines in Fig. 13 shows the variations of v_m^{ave} (*a*), η (*b*), $\Delta P/L$ (*c*), and CPC_{max} (*d*) with Re_f when $\hat{y}_c = 0.5$, and $\beta = 0.3$ (□), 0.5 (△), 0.7 (*). The dashed lines show results without spacers. Panels (*a*) and (*b*) show that vapor production and thermal efficiency improve with increasing blockage ratio when the feed Reynolds number is below $Re_f \leq 240$. However, for $Re_f \geq 250$, the performance of spacers with blockage ratio $\beta = 0.7$ suddenly drops due to the appearance of the steady bi-stable states. Panels (*c*) and (*d*) show that the increase in vapor production and efficiency with increasing blockage is countered by an increase in $\Delta P/L$ and CPC_{max}. At $Re_f = 300$, the pressure gradient for $\beta = 0.7$ is nearly 550% of that for $\beta = 0.3$. Note that CPC_{max} shows significant variations with Re_f due to the appearance of the bi-stable states.

Overall, the results in Fig. 13 suggest that when treating low-concentration feeds, one can increase vapor production and thermal efficiency by increasing the blockage ratio. However, at high blockage ratios, one must avoid the bi-stable steady states. When treating feeds for which mineral scaling is a risk, small blockage ratios may be preferred, because they delay transition to vortex shedding, such that there is a greater operating region with steady flow and decreased concentration polarization. When interpreting these results, it is worth noting that for typical diamond spacers used in industry and many lab settings, the spacer diameter varies widely along the filament length, and approaches 100% blockage at nodes where two filaments meet in a weld [25].

4.3. Influence of spacer offset $\hat{y}_c$

To investigate the spacer offset, we consider $\hat{y}_c = 0.3$ and 0.7, while maintaining the blockage ratio $\beta = 0.5$. Fig. 14(*a*) shows streamlines for $\hat{y}_c = 0.3$ when $Re_f = 800$. Placing the spacers near the membrane surface substantially delays transition to vortex shedding, such that both channel flows are steady, despite the large Reynolds numbers. Both channels have large membrane-vortices that cover the full membrane surfaces downstream from the spacers. In the feed channel, there is an additional vortex pair between the cylinder and the downstream membrane vortex. Note that there is a small gap between the cylinders and the membrane surfaces. Flow through this gap likely plays a role in the formation of the vortex pair in the feed channel, and may explain why the membrane-vortex in the distillate channel is displaced downstream from the cylinder surface. The zoom-in view upstream of the feed cylinder (indicated in the red box) shows that a small vortical structure forms on the membrane near $x/H = 4.5$. The structure appears because there is a region of diverging streamlines upstream of the cylinder, between the membrane surface and the streamline that terminates on the

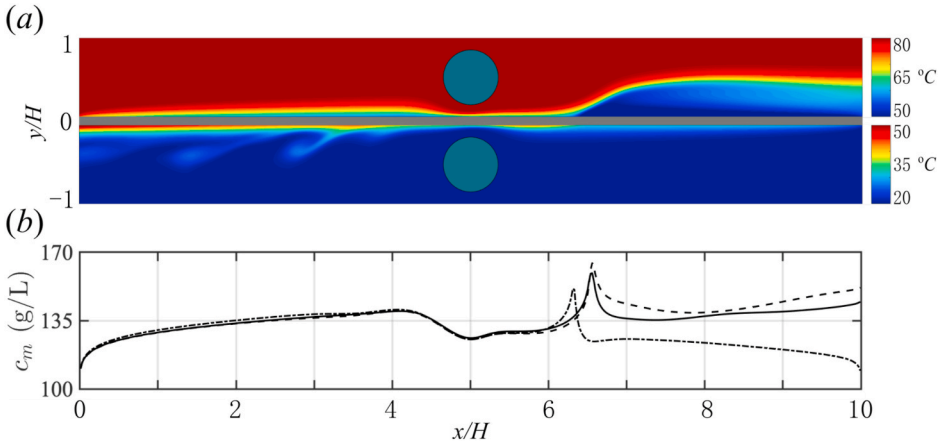

Fig. 12. (*a*) Temperature field when $\beta = 0.7$, $\hat{y}_c = 0.5$, and $Re_f = 300$. (*b*) Downstream variation of c_m for $\beta = 0.7$, $\hat{y}_c = 0.5$ when $Re_f = 200$ (solid), 240 (dashed), and 300 (dash-dotted).

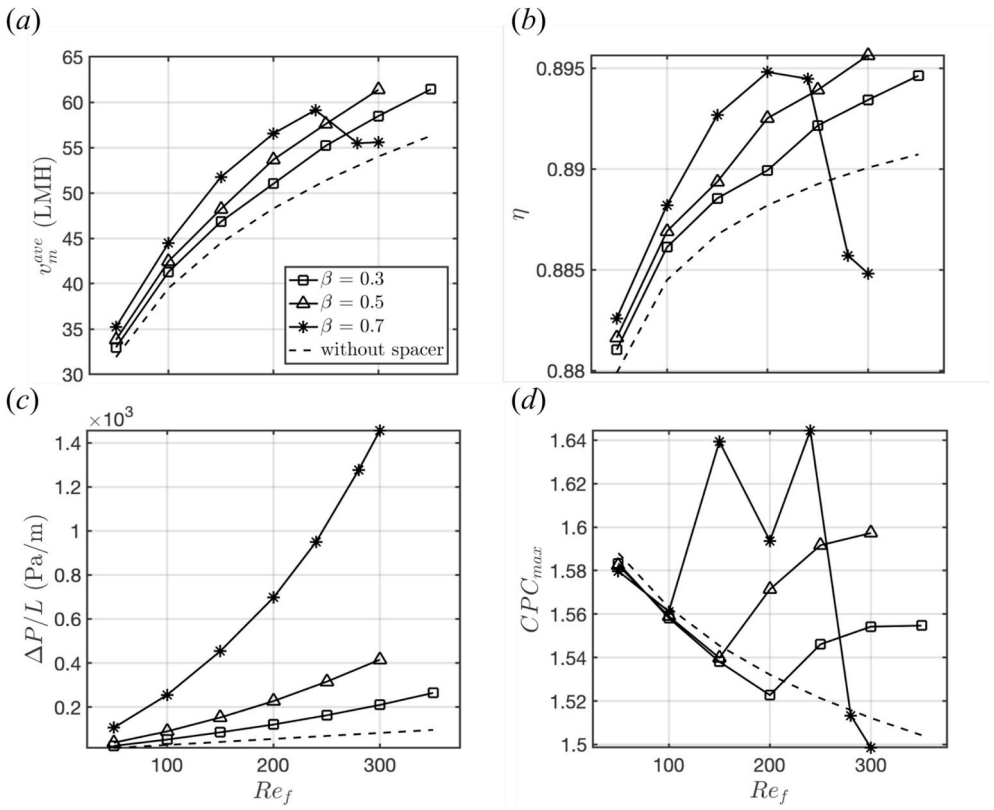

Fig. 13. The solid lines show the variations of (*a*) v_m^{ave}, (*b*) η, (*c*) $\Delta P/L$, and (*d*) CPC_{max} with Re_f when $\hat{y}_c = 0.5$, and $\beta = 0.3$ (□), 0.5 (△), and 0.7 (*). The dashed lines show the results for simulations without spacers.

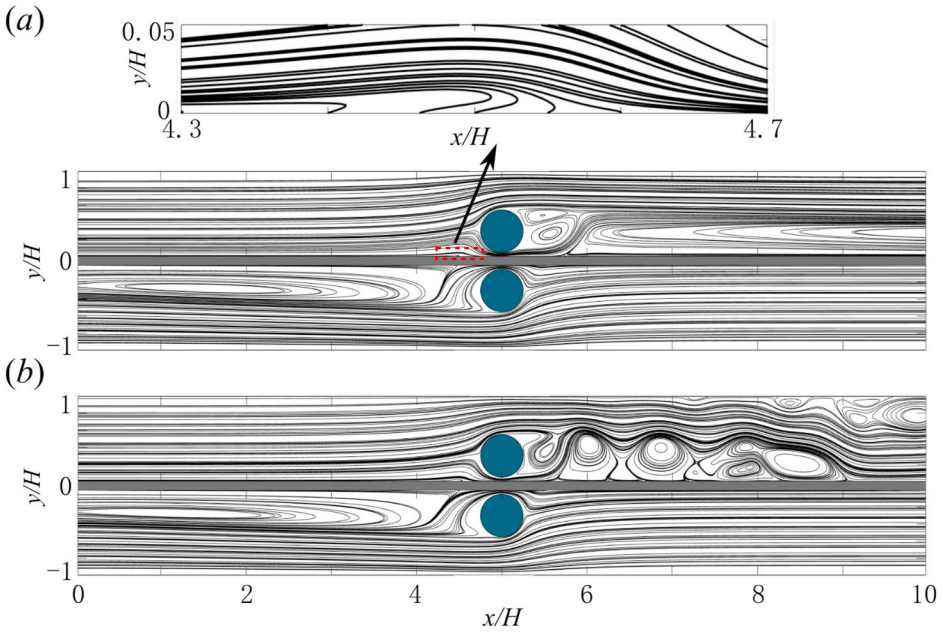

Fig. 14. Streamlines for $\hat{y}_c = 0.3$ when $Re_f = 800$ (*a*) and 900 (*b*), respectively. The zoom-in view in panel (*a*) shows the reverse flow upstream of the feed cylinder.

upstream edge of the cylinder. Fig. 14(*b*) shows streamlines when the feed Reynolds number is increased to $Re_f = 900$. (Additional simulations estimate the critical Reynolds number $Re_c = 895$.) The feed flow is unsteady, with large vortical structures traveling along the membrane and outer plate. The membrane-vortices are generated immediately behind the cylinder, while the plate-vortices appear further downstream, near $x/H = 7$.

Fig. 15 shows corresponding temperature and concentration fields when $Re_f = 800$ (*a* and *b*), and 900 (*c* and *d*). Panel (*a*) shows that the steady membrane-vortices significantly exacerbate temperature polarization, forming a large region of recirculating cool fluid in the downstream feed channel, and a similar region of recirculating warm fluid in the distillate channel. Panel (*b*) shows that regions of salt accumulation form not only downstream of the cylinder, but also at the upstream

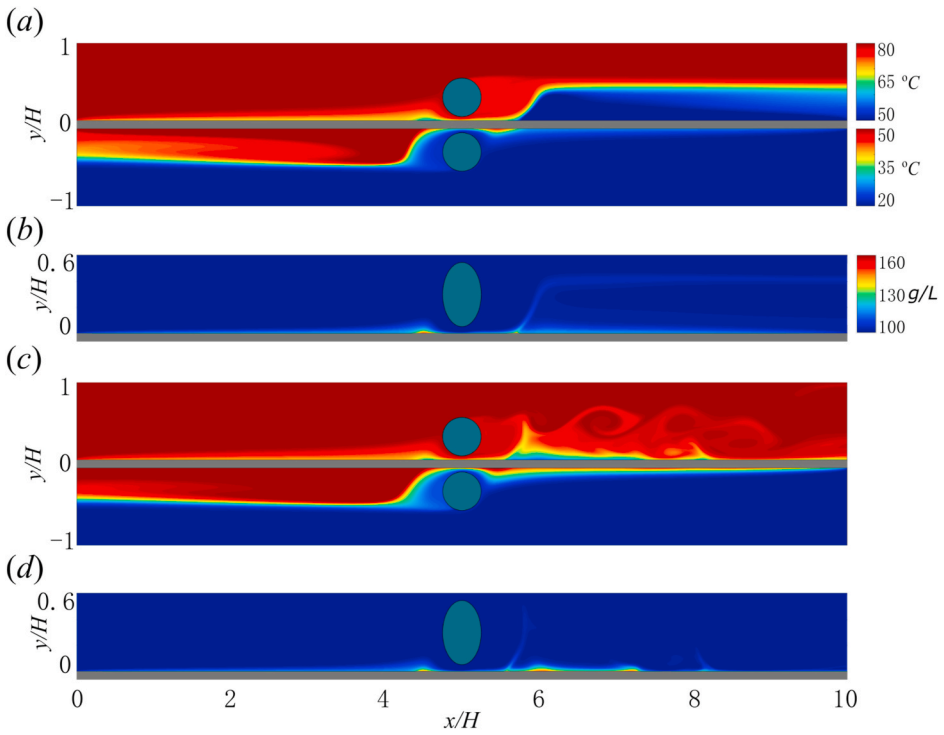

Fig. 15. Temperature and concentration fields for $\hat{y}_c = 0.3$ when $Re_f = 800$ (*a* and *b*), and 900 (*c* and *d*), respectively. Note that the concentration field is shown for $0 < y/H < 0.6$.

location $x/H = 4.5$ due to the vortical structure shown in Fig. 14(*a*). Fig. 15(*c*) shows that the appearance of large energetic membrane-vortices strongly mix the thermal boundary layer. However, panel (*d*) shows that these membrane-vortices also generate several downstream regions of salt accumulation. Overall, the results in Fig. 15 and earlier in Fig. 12, show that stationary membrane-vortices exacerbate both temperature and concentration polarization. Only translating membrane-vortices reduce temperature polarization, albeit at the expense of concentration polarization.

Fig. 16 shows the streamlines (*a*), temperature field (*b*), and concentration field (*c*) when the cylinders are near the outer plates ($\hat{y}_c = 0.7$) and $Re_f = 800$. Panel (*a*) shows that the streamlines are essentially the mirror image of those for $y_c = 0.3$ in Fig. 14(*a*). The feed and distillate flows accelerate between the spacers and the membrane, thereby decreasing temperature and concentration polarization, such that the spacers have a net beneficial effect. Fig. 17 shows corresponding results when $Re_f = 900$. The acceleration of the feed and distillate flows between the spacers and membrane once again reduces polarization phenomena in a region downstream of the cylinders. However, the appearance of membrane-vortices further downstream, near $x/H = 7$,

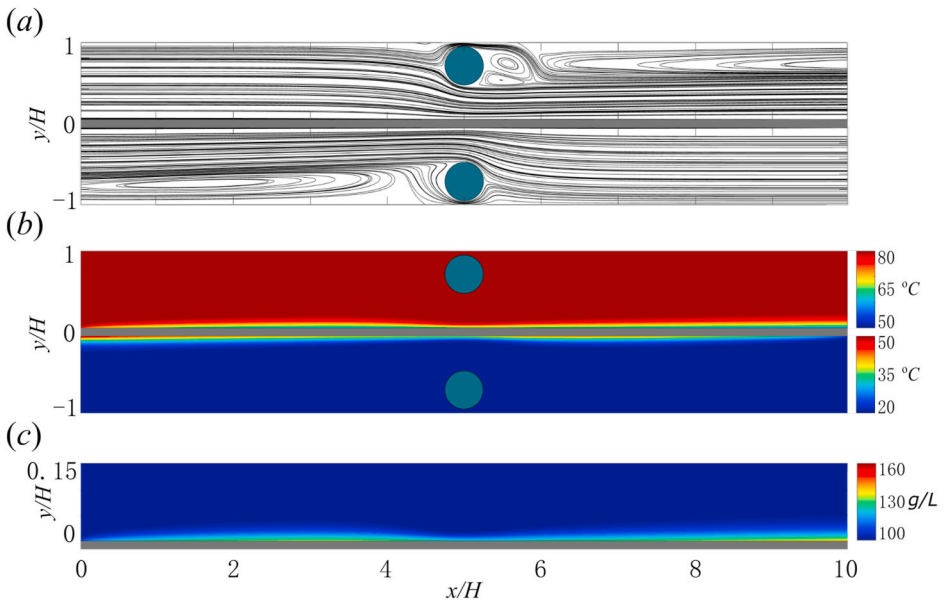

Fig. 16. Streamlines (*a*), temperature field (*b*), and concentration field (*c*) when $\hat{y}_c = 0.7$ and $Re_f = 800$. Note that the concentration field is shown for $0 < y/H < 0.15$.

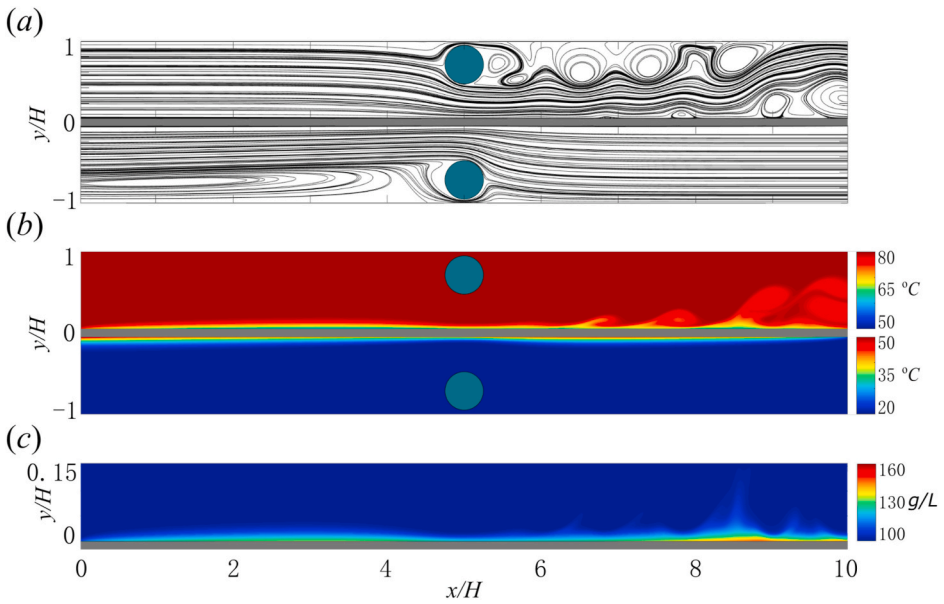

Fig. 17. Streamlines (*a*), temperature field (*b*), and concentration field (*c*) when $\hat{y}_c = 0.7$ and $Re_f = 900$. Note that the concentration field is shown for $0< y/H <0.15$.

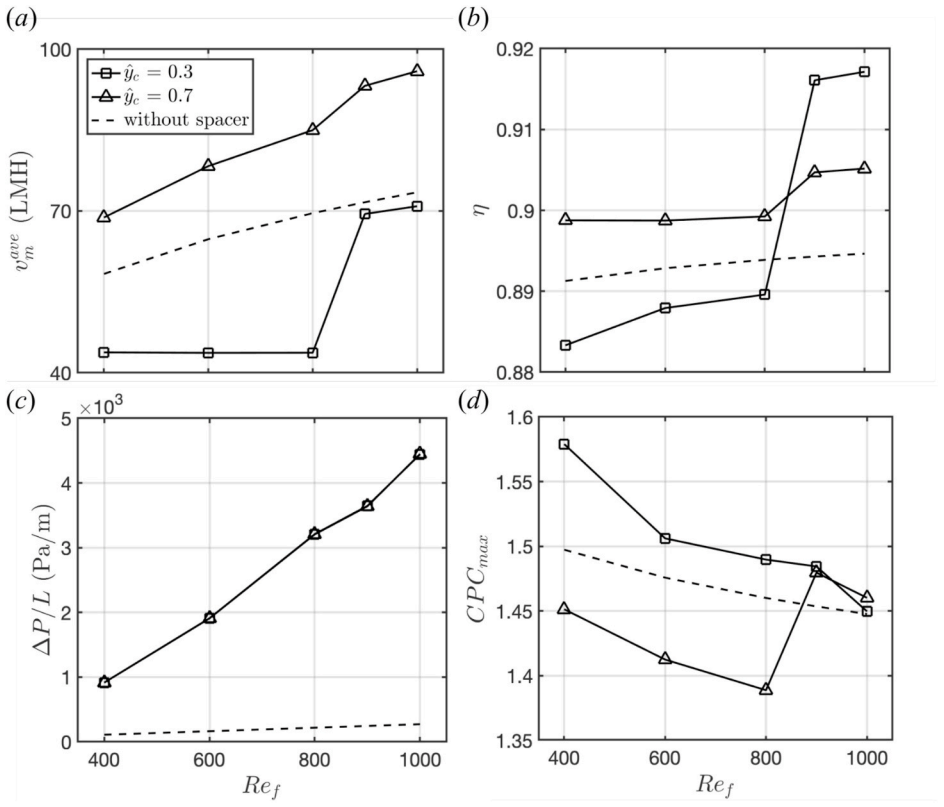

Fig. 18. The solid lines show the variations of (*a*) v_m^{ave}, (*b*) η, (*c*) $\Delta P/L$, and (*d*) CPC_{max} with Re_f for $\hat{y}_c = 0.3$ (□) and 0.7 (△). The dashed lines show corresponding results without spacers.

mixes the temperature layer and causes salt accumulation near $x/H = 9$. Additional results for ΔT_m, c_m, and ν_m are presented in appendix E.

The solid lines in Fig. 18 shows the variations of (*a*) v_m^{ave}, (*b*) η, (*c*) $\Delta P/L$, and (*d*) CPC_{max} with Re_f for $\hat{y}_c = 0.3$ (□) and 0.7 (△). The dashed lines show corresponding results without spacers. Panel (*a*) shows that spacers placed near the outer plates ($\hat{y}_c = 0.7$) always produce more v_m^{ave} than systems without spacers. In contrast, spacers near the membrane ($\hat{y}_c = 0.3$) always produce less, particularly in the steady regime. Panel (*b*) shows that η increases substantially for $\hat{y}_c = 0.3$ and 0.7 after transition to vortex shedding ($Re_f \leq 900$) due to the sudden increase in v_m^{ave}. Panel (*c*) shows that $\hat{y}_c = 0.3$ and 0.7 essentially produce the same pressure drop at different Re_f due to their symmetry along the channel centerlines. Panel (*d*) shows that $\hat{y}_c = 0.7$ decreases CPC_{max} in the steady regime. However, transition to vortex shedding causes a sudden increase

in CPC_{max}, exceeding that observed without spacers. Finally, we observe that $\hat{y}_c = 0.3$ always increases CPC_{max} in comparison to that without spacers.

When interpreting the results of spacers placed near an outer feed plate, it is worth noting that future industrial DCMD systems might replace the feed plate with a second membrane. In that case, a spacer filament placed near one of the membrane surfaces will increase concentration polarization on that membrane, while decreasing concentration polarization on the opposite membrane. Furthermore, for the diamond spacers used in industry, the displacement $\hat{y}_c$ of a filament varies along the membrane surface. For the scope of this exploratory 2D study, we do not consider the impact of a second membrane. However, the results of our parametric study show that the presence of a membrane has a negligible impact on the flow regime, as shown in Table 1, and is unlikely to produce significant new physical insights from those observed here with a single membrane.

4.4. Influence of multiple spacers

A detailed parametric study of multiple cylinders in the feed and distillate channels is beyond our scope. We nevertheless consider two select cases to determine whether our observations for single spacer filaments will likely extend to systems with multiple filaments. For that purpose, we place three equispaced cylinders in both channels at $x/H =$ 2.5, 5, and 7.5, thereby maintaining a distance of 2.5 diameters between each cylinder. All spacers have a blockage ratio of $\beta = 0.5$, and we fix the flow rates such that $Re_f = 300$.

Fig. 19(*a*) shows streamlines when all spacers are placed on the centerlines ($\hat{y}_c$=0.5). In the feed channel, the downstream propagation of shedding vortices is interrupted by the downstream cylinders. Panel (*b*) shows that in the feed channel, the cool fluid ejected by membrane-vortices further couples with the downstream spacers, producing stronger mixing with the bulk. Panel (*c*) shows three major regions of salt accumulation near $x/H =$ 4, 6, and 8.5 due to the leading membrane-vortex behind each spacer. Fig. 20 shows corresponding downstream variation of ΔT_m (*a*), c_m (*b*), and v_m (*c*). As predicted by our analysis of single spacer filaments, ΔT_m and v_m increase near the cylinders, but at the expense of salt accumulation near $x/H =$ 3.8, 6, and 7.8.

To investigate staggered cylinders, we first consider Fig. 21(*a*) showing streamlines in a system with a single cylinder placed in each channel at $L/H = 5$ and $\hat{y}_c = 0.3$. We then consider Fig. 21(*b*) showing streamlines when additional cylinders are placed near the outer plates ($\hat{y}_c = 0.7$) at $L/H = 2.5$ and 7.5. The additional spacers redirect the flow such that the central spacers have a much larger upstream membrane-vortex and much smaller downstream-vortex. Fig. 21(*c*) and (*d*) consequently show strong temperature and concentration polarization both upstream and downstream of the central spacer. Fig. 22 shows the downstream variation of ΔT_m (*a*), c_m (*b*), and v_m (*c*) for the cases in Fig. 21(*a*) and (*b*). Panels (*a*) and (*c*) show that due to the smaller downstream membrane-vortices, the staggered arrangement shows increased ΔT_m and v_m compared to the single spacer case. Panel (*b*) shows that the upstream local salt accumulation for the staggered case occur at $x/H = 4$ due to a larger upstream membrane-vortex.

Overall, our brief consideration of multiple spacers suggests that the fundamental mechanisms we observed for single filaments help explain what occurs in systems with multiple spacers. We do not perform a more detailed parametric study of multiple spacer arrangements, because it is our philosophy that 3D effects are also required for such analysis.

5. Conclusions

The impact of 2D spacers on polarization can be physically explained by examining the variety of vortical structures generated in steady and unsteady flow regimes. The impact of these structures on polarization depends on whether the structures occur in the bulk, on the membrane surface, or on the outer plate, and whether they are steady (as in subcritical regimes, $Re < Re_c$) or translate downstream (as in supercritical regimes, $Re > Re_c$). In steady regimes, vortical structures decrease both temperature and concentration polarization when the structures occur in the bulk or on the outer plates. In those cases, the structures accelerate and redirect bulk fluid towards the membrane surface. Steady vortical structures can be generated in the bulk by placing filaments on the channel centerline ($\hat{y}_c = 0.5$). In that case, the reduction of temperature and concentration polarization increases with the blockage ratio β, but at the expense of increasing pumping costs. Increasing the blockage ratio also decreases the critical Reynolds number Re_c. This limits the range of flow rates for which one can decrease both temperature and concentration polarization. Vortical structures can be generated on the outer plate by placing the spacer filament near the plate. In that case, the vortical structures grow with Reynolds

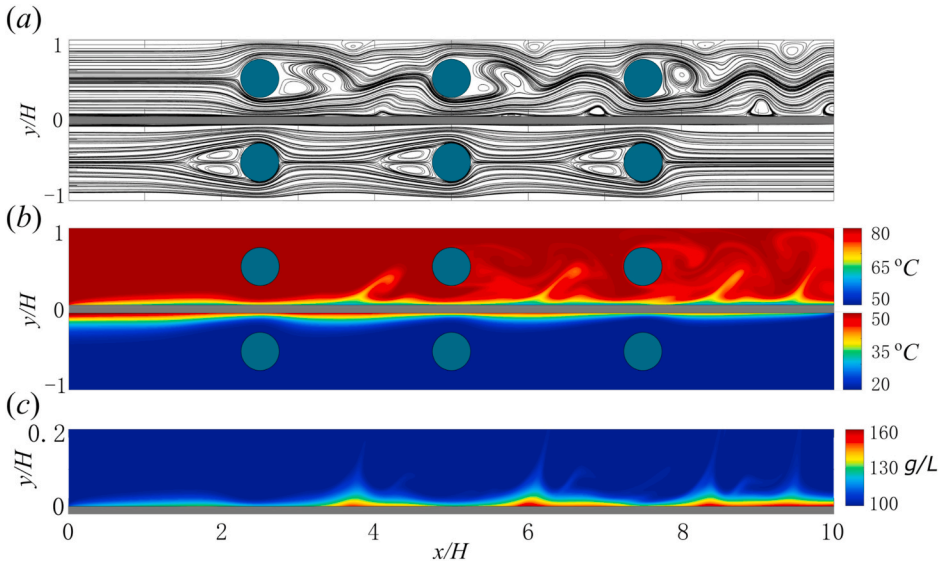

Fig. 19. Results when each channel has three spacers on the centerline. (*a*) Streamlines. (*b*) Temperature field. Different color scales are used in the distillate and feed channels. (*c*) Feed concentration field for $0< y/H <0.2$. (For interpretation of the references to color in this figure legend, the reader is referred to the Web version of this article.)

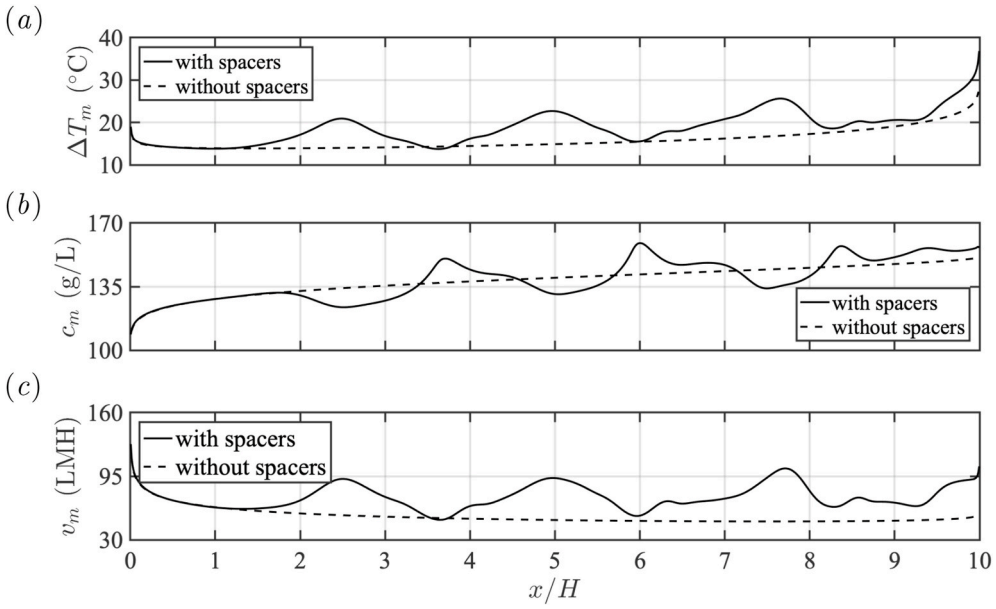

Fig. 20. Downstream variation of ΔT_m (*a*), c_m (*b*), and v_m (*c*) when all spacers are placed on the centerline.

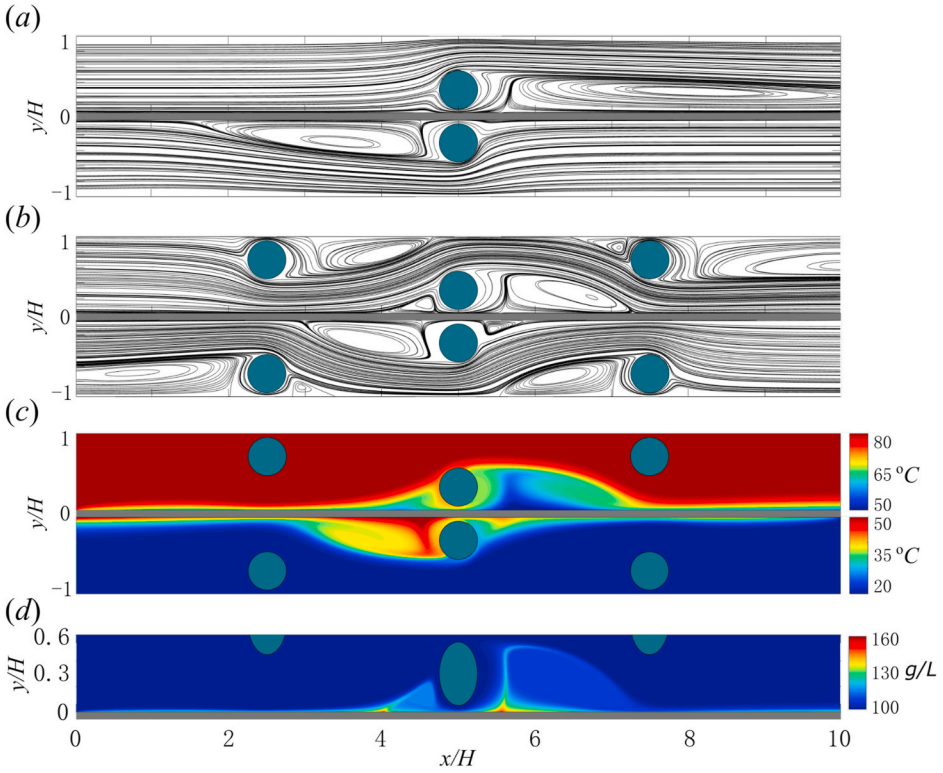

Fig. 21. (*a*) Streamlines for single spacers near the membrane ($\hat{y}_c = 0.3$). Streamlines (*b*), temperature field (*c*), and concentration field (*d*) for three spacers placed at $\hat{y}_c = 0.7$, 0.3, and 0.7, respectively.

number, and the critical Reynolds number is $Re_c \sim 900$, providing a wider range of flow rates for which one can leverage the decrease in polarization.

In contrast to steady vortical structures in the bulk or on the outer plate, steady vortical structures on the membrane surface increase both temperature and concentration polarization. This occurs when spacer filaments are placed near the membrane surface. Temperature polarization increases because the closed streamlines of the structures inhibit heat transfer with the bulk. Concentration polarization increases because the structures advect solutes upstream, where they accumulate

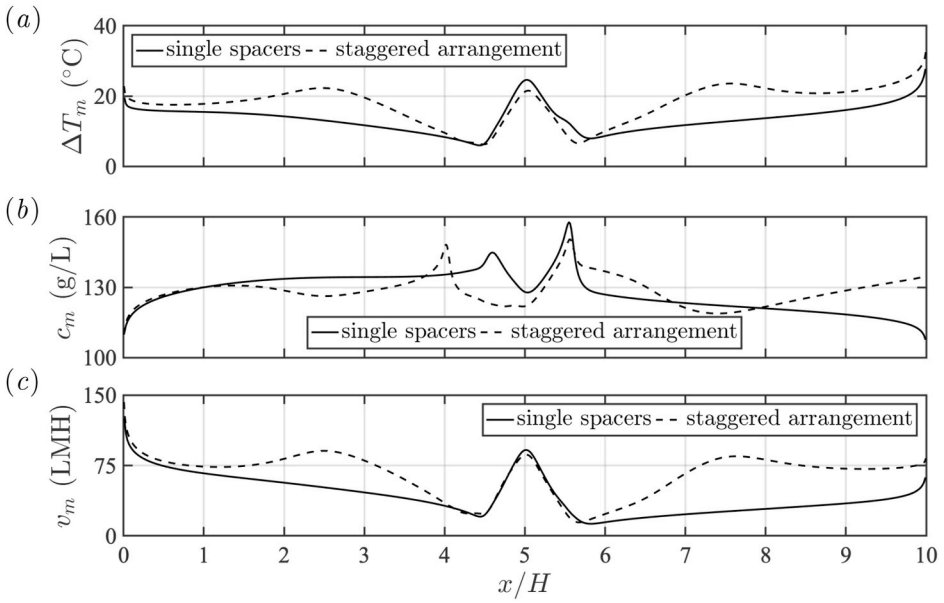

Fig. 22. Downstream variation of ΔT_m (*a*), c_m (*b*), and v_m (*c*) for the cases in Fig. 21(*a*) and (*b*).

at the leading edge of the vortex.

Throughout our study, we found that the small transmembrane velocity component had a negligible impact on the critical Reynolds numbers for transition to vortex shedding, compared to what is observed when the membrane is replaced with an impermeable wall. Transition to vortex shedding generates an unsteady procession of staggered vortices in the bulk as well as vortical structures that travel downstream along the membrane surface. The translating membrane-vortices mix the thermal layers and decrease temperature polarization, but do not similarly mix the concentration layers. Rather, they form regions of salt accumulation at the vortex leading edge. We hypothesize that this behavior is due to the fact that the concentration layers are very thin compared to the thermal layers. This in turn is due to the low mass diffusivity of the salts. Vortex shedding consequently tends to decrease temperature polarization at the expense of increasing concentration polarization.

We also note that for large blockage ratios ($\beta = 0.7$), the vortex shedding regime can be followed by a transition to a bi-stable steady state with large membrane-vortices. These bi-stable states should be avoided because they increase both temperature and concentration polarization.

Overall, our results show that optimal operating conditions and spacer designs depend on the feed conditions. When treating low-concentration feeds, vortex shedding is preferable because it increases vapor production. In that case one should design spacers to minimize the critical Reynolds number Re_c. Conversely, when treating high-concentration feeds with risk of mineral scaling, it may be safer to operate in a steady regime without membrane-vortices. Ongoing work now focuses on simulating 3D spacers. In that regard, we note that hydrodynamic instabilities are sensitive to whether a simulation is 2D or 3D. We consequently expect that the critical Reynolds numbers and flow regimes may change from those reported here. We nevertheless expect 3D spacers to generate vortical structures that are able to mix the thick thermal boundary layers at the expense of concentrating solutes within the thin concentration boundary layers. The results of the current study are also the topic of an ongoing experimental study. The experiments use a plate-and-frame DCMD system in which single spacer filaments are suspended across the side-walls of the feed and distillate channels to recreate the flow conditions studied here.

Author statement

Jincheng Lou: Conceptualization, Methodology, Software,Formal Analysis, Writing. **Jacob Johnston**: Methodology, Software, Validation, Formal Analysis, Writing-Review & Editing. **Tzahi Y. Cath:** Conceptualization, Resources, Writing-Review & Editing, Funding Acquisition. **Denis Martinand:** Conceptualization, Resources, Writing-Review & Editing. **Nils Tilton:** Supervision, Conceptualization, Methodology, Writing, Funding Acquisition, Resources.

Declaration of competing interest

The authors declare that they have no known competing financial interests or personal relationships that could have appeared to influence the work reported in this paper.

Acknowledgements

This work was generously supported by the Colorado School of Mines Slater Family Research Fund, the U.S. Bureau of Reclamation (R16AC00121), the Colorado Office of Economic Development and International Trade, a National Science Foundation CAREER Award (1752531), and the Embassy of France Thomas Jefferson Fund. The authors thank Dr. John Farnsworth (University of Colorado, Boulder) for helping interpret vortical flow structures. We also thank Drs. Tony Saad (University of Utah), Amneet Pal Bhalla (San Diego State University), Amir Riaz (University of Maryland), and Drs. Paul Martin and Greg Fasshauer (Colorado School of Mines) for aiding our code development.

Appendix

A. Numerical method

In all simulations, the cells in the y-direction are concentrated near the membrane and outer plate using Gauss-Lobatto points in both channels,

$$y_i = -(H/2)\cos(\pi i / N_y), \quad i = 0, 1, \ldots, N_y, \tag{17}$$

where N_y is the number of cells in the y-direction. For the simulations with multiple spacers in section 4.4, the cells are equispaced cells in the x-direction. For all other simulations, we refine the grid near the cylinder by decomposing the x-direction into three sections, as demonstrated in Fig. 23. A core section of length $L_1 = \mathrm{H}$ is centered about the cylinder, and has N_1 equispaced cells. The inlet section has a length L_2 and N_2 equispaced cells. The outlet section has a length L_3 and N_3 equispaced cells.

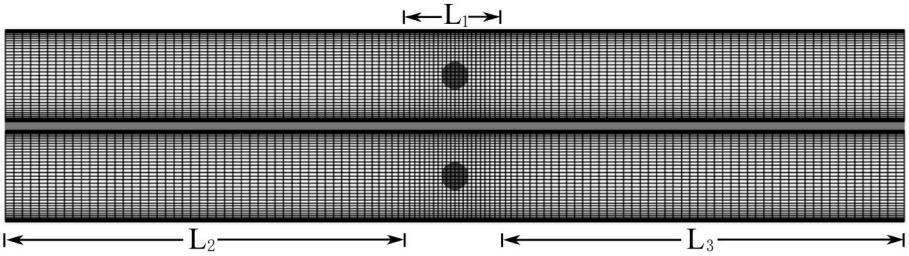

Fig. 23. Sketch that demonstrates mesh grids for simulated DCMD system for $N_x = 120$, $N_y = 40$. We typically concentrate grid points near the membrane, outer plate, and spacers to capture the rapid variations in boundary layers.

A.1. Code benchmarking

Using standard practice in CFD, we verify the temporal and spatial accuracies of our discretization with respect to the following analytical solution,

$$\begin{aligned} &c_e = \sin(x)y^2\cos(\omega t), \quad p_e^f = p_e^d = \sin(x)\sin(y)\cos(\omega t), \\ &T_e^f = 3/\pi\cos(x)y^2\cos(\omega t), \quad T_e^d = 1/\pi\cos(x)y^2\cos(\omega t), \\ &u_e^f = -\sin(x)\cos(\pi y/2)\cos(\omega t), \quad u_e^d = \sin(x)\cos(\pi y/2)\cos(\omega t), \\ &v_e^f = 2/\pi\cos(x)\sin(\pi y/2)\cos(\omega t), \quad v_e^d = -2/\pi\cos(x)\sin(\pi y/2)\cos(\omega t) \end{aligned} \tag{18}$$

which satisfies the governing equations with the addition of appropriate forcing terms. The numerical solvers were tested with the feed and distillate channels coupled, subject to general Robin boundary conditions of the form

$$a g^{n+1} + b\nabla g^{n+1}\cdot\mathbf{s} = q, \tag{19}$$

where $g = [\mathbf{u}, T, c]$, is the velocity, temperature, or concentration field, a and b are constant coefficients, $\mathbf{s}$ is the normal to the boundary, and q is the appropriate boundary source terms determined from the solution (18).

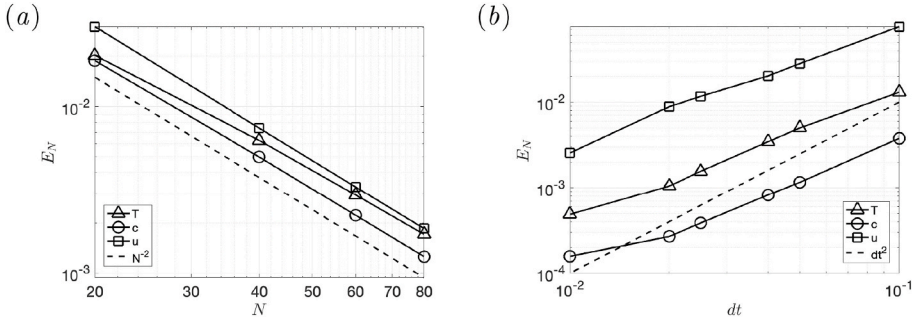

Fig. 24. (a) Variation of spatial error E_N for temperature (T), u component (u) and pressure (p) as function of grid number N. (b) Variation of temporal error E_t for temperature (T), u component (u) and pressure (p) as function of time size dt.

To test the spatial accuracy of the method, we set $L = 4$, $H = 2$, $D_{sp} = 1$, $y_c = 2$, $N_x = N_y = N$, $\omega = 0$, $g^0 = 0$ and integrate in time using N finite volumes in each direction (N^2 in total) until steady state, after which we evaluate the spatial error as $E_N = ||g - g_e||_\infty$. Fig. 24(a) demonstrates second-order spatial accuracy. To test temporal accuracy, we set $L = 3$, $H = 2$, $N_x = 120$, $N_y = 80$, $\omega = \pi$, and $g^0 = g_e^0$. The fields are integrated from t = 0 to 1 s for $0.01 \le dt \le 0.1$. Fig. 24(b) confirms second-order temporal accuracy.

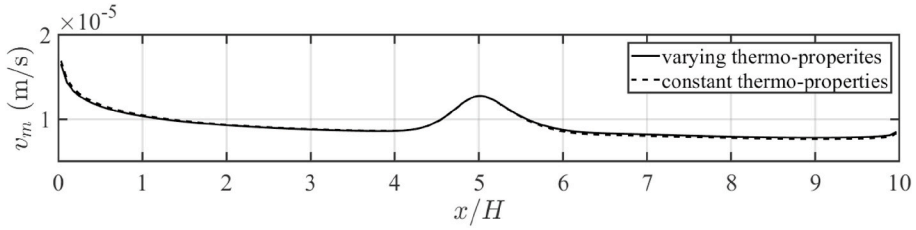

Fig. 25. Transmembrane vapor flux v_m for $N_x = 160$, $N_y = 80$, $\beta = 0.5$, $\widehat{y}_c = 0.5$, and $Re_f = 100$ when thermo-physical variations are included (solid line) and neglected (dashed line).

In our previous work [14], we include the variations of all thermo-physical properties, except density, with temperature and salt concentration, $\mu(T,c)$, $c_p(T,c)$, $\lambda(T)$, $k(T,c)$ and $D(T)$. For the short systems included in the current study, we found these variations had only a small quantitative effect, on the order of 1%. This is demonstrated in Fig. 25, comparing v_m for $N_x = 160$, $N_y = 80$, $\beta = 0.5$, $\widehat{y}_c = 0.5$, and $Re_f = 100$ when thermo-physical variations are included (solid line) and neglected (dashed line). Note here we set $B = 1 \times 10^{-6}$ kg/m^2 s Pa, so v_m is smaller than that shown in Fig. 6.

A.2. Grid independence study

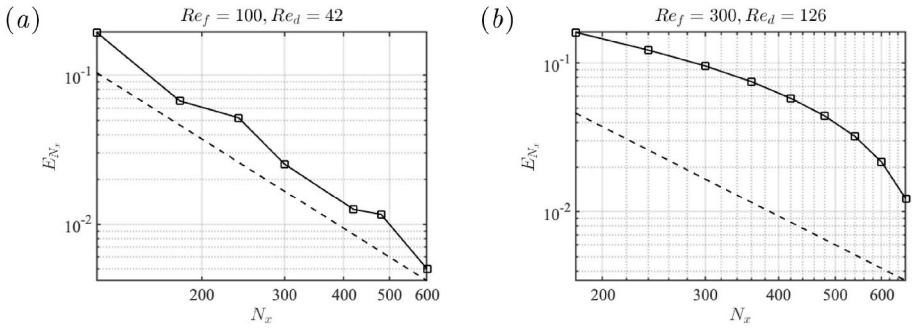

Fig. 26. (*a*) The solid line shows the variation of relative error of v component E_{N_x} with N_x at $Re_f = 100$ and $Re_d = 42$. (*b*) The solid line shows the variation of relative error of v component on the membrane Eb_{N_x} with N_x at $Re_f = 300$ and $Re_d = 126$.

We performed numerous grid independence studies to ensure the spatial accuracy of our results. Fig. 26(*a*) shows the results of one such study, performed for $U_{in} = 0.021$ m/s, $\beta = 0.5$, $\widehat{y}_c = 0.5$. This produces a steady case characterized by $Re_f = 100$ and $Re_d = 42$. To explore the effects of grid resolution, we first fix the ratio of grid resolution in the x and y directions as $N_x/N_y = 3:1$. We then vary N_x between $90 \leq N_x \leq 750$. We evaluate the relative error as

$$E_{N_x} = \frac{||g_{N_x} - g_{750}||}{||g_{750}||}, \tag{20}$$

where $g_{N_x} = [\mathbf{u}_{N_x}, T_{N_x}, c_{N_x}]$ is the solution evaluated at grid number N_x, and g_{750} is the solution at $N_x = 750$. Fig. 26(*a*) shows the resulting variation of the error in the plate-normal velocity field v. Fig. 26(*a*) shows the error is below 1% when $N_x = 600$. Fig. 26(*b*) shows corresponding results for a case where $Re_f = 300$ and $Re_d = 126$. In this case, the feed flow is unsteady. We consequently measure error using flow fields on the membrane surface, where v, T, and c are all quasi-steady. Fig. 26(b) shows the error is around 2% when $N_x = 600$. For unsteady cases, we ensured temporal accuracy by ensuring the time step was at least one hundred times smaller than the period of vortex shedding.

B. Thermal and concentration boundary layer thickness

To measure the thermal boundary layer thickness in the feed channel, we define the non-dimensional temperature $\widehat{T}$ and coordinates $\widehat{x}$ and $\widehat{y}$ as

$$\widehat{T}(x,y) = \frac{T(x,y) - T_m^f(x)}{T_{in}^f - T_m^f(x)}, \quad \widehat{x} = \frac{x}{H}, \quad \widehat{y} = \frac{y}{H}. \tag{21}$$

$\widehat{T}$ is defined such that it varies from zero on the membrane surface ($\widehat{y} = 0$) to unity when $T = T_{in}^f$. We then define the non-dimensional thermal boundary layer thickness $\widehat{\delta}_T(\widehat{x})$ as the location where

$$\widehat{T}|_{\widehat{y}=\widehat{\delta}_T(\widehat{x})} = 0.95. \tag{22}$$

We similarly define the non-dimensional concentration

$$\widehat{c} = \frac{c - C_{in}}{c_m(x) - C_{in}}. \tag{23}$$

We then define $\widehat{\delta}_c(\widehat{x})$ as the location where

$$\widehat{c}|_{\widehat{y}=\widehat{\delta}_c(\widehat{x})} = 0.05. \tag{24}$$

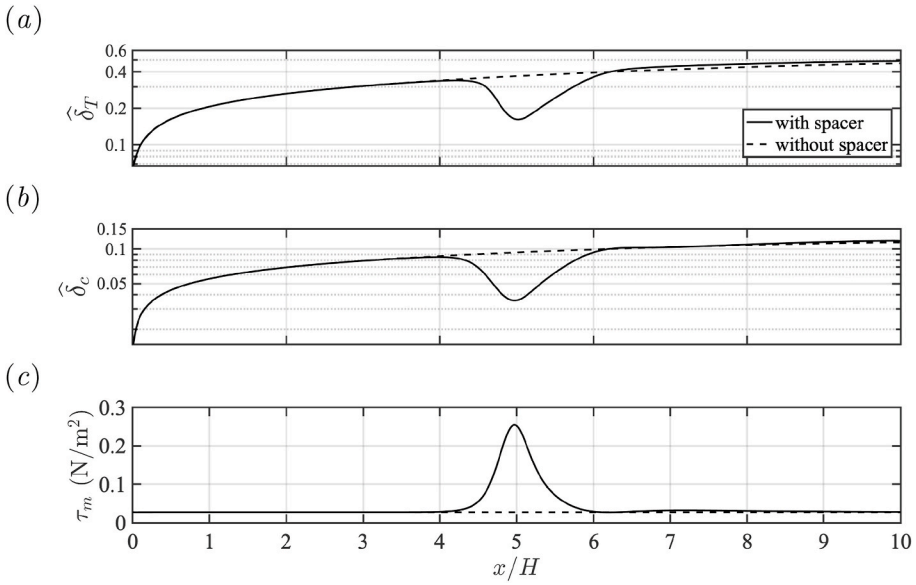

Fig. 27. The solid lines show the downstream variation of (*a*) $\widehat{\delta}_T$, (*b*) $\widehat{\delta}_c$, and (*c*) the feed membrane surface shear stress $\tau_m = \mu \partial u/\partial y$. The dashed lines show corresponding results without spacers.

Fig. 27 shows the downstream variation of $\widehat{\delta}_T$ (panel *a*) and $\widehat{\delta}_c$ (panel *b*) measured in the feed channel for the simulation shown in Fig. 5 ($\beta = 0.5$, $\widehat{y}_c = 0.5$, and $Re_f = 100$). The solid line in panel (*c*) shows the downstream variation of the shear stress on the feed side of the membrane $\tau_m = \mu \partial u/\partial y$. In all panels of Fig. 27, the dashed lines show corresponding results when the simulation is run without spacers. Consistent with our discussion of Fig. 5, the boundary layer thicknesses decrease from those observed without spacers. We also see a sharp increase in the membrane shear stress. However, the influence of the spacer is limited to a region extending roughly two cylinder diameters up and downstream from the cylinder center.

C. Evolution of the membrane-vortices for $\widehat{y}_c = 0.5$ and $\beta = 0.5$

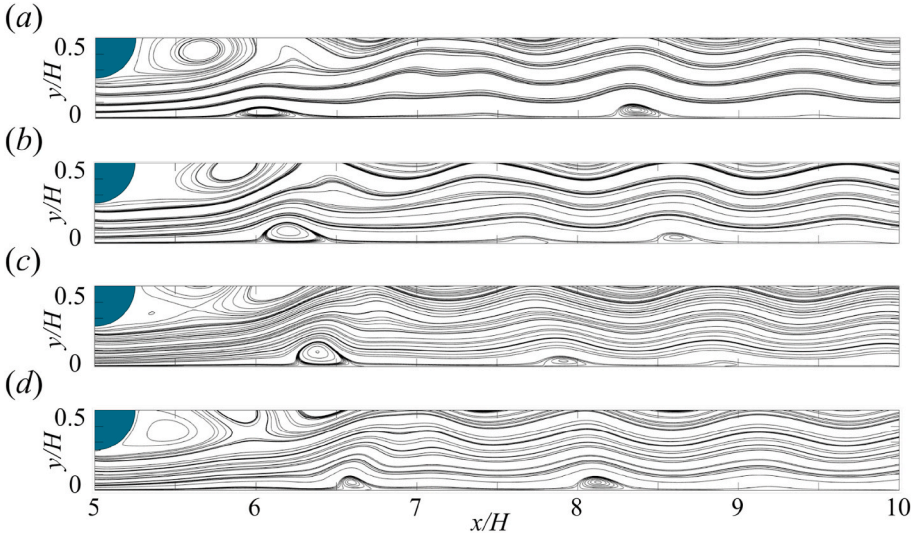

Fig. 28. Instantaneous streamlines downstream of the feed spacer for $\widehat{y}_c = 0.5$ and $\beta = 0.5$ when $Re_f = 300$ and $Re_d = 126$. Panel (*a*), (*b*), (*c*), and (*d*) show results at $t = 0$, T/4, T/2, and 3T/4, respectively, where T is the period for vortex shedding.

Fig. 28 shows sequential snapshots of the streamlines in the downstream feed channel for $\hat{y}_c = 0.5$ and $\beta = 0.5$ when $Re_f = 300$ and $Re_d = 126$. Membrane-vortices periodically form at multiple downstream locations, initially growing as they travel downstream, before dissipating. The first vortex forms near $x/H = 6.1$, and dissipates near $x/H = 6.7$. Our inspection of the pressure field suggests that the leading membrane-vortex forms due to an adverse pressure gradient, $\partial p/\partial x > 0$, in the downstream region of the feed spacer. This adverse gradient occurs due to the rapid expansion of cross-sectional flow area over the rear surface of the spacer. Additional adverse gradients occur along the downstream membrane surface due to interactions between the membrane and vortical structures in the bulk flow.

D. Order-of-magnitude analysis for near-membrane solute advection

As mentioned in section 4.1, we observed that the concentration on the membrane surface remains essentially steady for cases of vortex shedding. To understand this result physically, we consider the advection-diffusion equation (9) at the feed surface of the membrane

$$\frac{\partial c_m}{\partial t} + u_m \frac{\partial c_m}{\partial x} + v_m \frac{\partial c_m}{\partial y} = D\frac{\partial^2 c_m}{\partial x^2} + D\frac{\partial^2 c_m}{\partial y^2}, \tag{25}$$

where the subscript m stresses that we are considering the equation on the membrane surface. This equation can be simplified by setting $u_m = 0$ and neglecting $\partial c_m^2/\partial x^2$, which our simulations showed to be two orders-of-magnitude smaller than $\partial c_m^2/\partial y^2$. This produces,

$$\frac{\partial c_m}{\partial t} + v_m \frac{\partial c_m}{\partial y} = D\frac{\partial^2 c_m}{\partial y^2}. \tag{26}$$

To estimate the order-of-magnitudes of the three terms in Eqn. (26), we scale derivatives of c with y as

$$\frac{\partial c_m}{\partial y} \sim \frac{\Delta C}{\overline{\delta}_c}, \quad \frac{\partial^2 c_m}{\partial y^2} \sim \frac{\Delta C}{\overline{\delta}_c^2}, \tag{27}$$

where $\Delta C = \overline{C}_m - C_{in}$, $\overline{C}_m$ is the average concentration on the membrane surface, and $\overline{\delta}_c$ is the average thickness of the concentration boundary layer. We scale the derivative $\partial c_m/\partial t$ as

$$\frac{\partial c_m}{\partial t} \sim \frac{\Delta C}{\tau_m}, \tag{28}$$

where τ_m is some characteristic time scale (to be determined) of temporal variation of c at the membrane surface. Finally, we scale v_m as $v_m \sim \overline{V}_m$, where $\overline{V}_m$ is the average velocity v at the membrane feed surface.

With these dimensional scales, we scale Eqn. (26) as,

$$\frac{\Delta C}{\tau_m} \sim \frac{V_m \Delta C}{\overline{\delta}_c} + \frac{D\Delta C}{\overline{\delta}_c^2}. \tag{29}$$

By multiplying Eqn. (29) with $H/(U_{in}\Delta C)$, we obtain the Strouhal number St_m for c_m as,

$$St_m = \frac{H}{U_{in}\tau_m} \sim \frac{V_m}{U_{in}}\frac{H}{\overline{\delta}_c} + \frac{1}{Pe}\left(\frac{H}{\overline{\delta}_c}\right)^2, \quad Pe = \frac{U_{in}H}{D}, \tag{30}$$

where Pe is the Peclet number. The typical Peclet number in our simulations is $Pe \approx 30000$. We estimate $V_m/U_{in} \approx 5 \times 10^{-4}$ and $H/\overline{\delta}_c \approx 10$ from Figs. 6(c) and Fig. 27(b), respectively. Consequently, we estimate $St_m \sim 1 \times 10^{-2}$. From Table 1, we see that the Strouhal number for vortex shedding, St, is typically on the order of 1. From the definition of Strouhal number, the characteristic time scale τ_m is estimated as,

$$\tau_m = \frac{St}{St_m}\tau_b \sim 100\tau_b, \tag{31}$$

where τ_b is the period for vortex shedding in the bulk flow. Finally, we conclude that because the bulk flow characteristic time length τ_b is much smaller than the membrane characteristic time length τ_m, c_m is not able to reflect the strong unsteadiness of the bulk flow, showing negligible variation in time. Similar analysis can be done for the membrane surface temperature.

E. Downstream variation of ΔT_m, c_m, and v_m for $\hat{y}_c = 0.3$ and 0.7

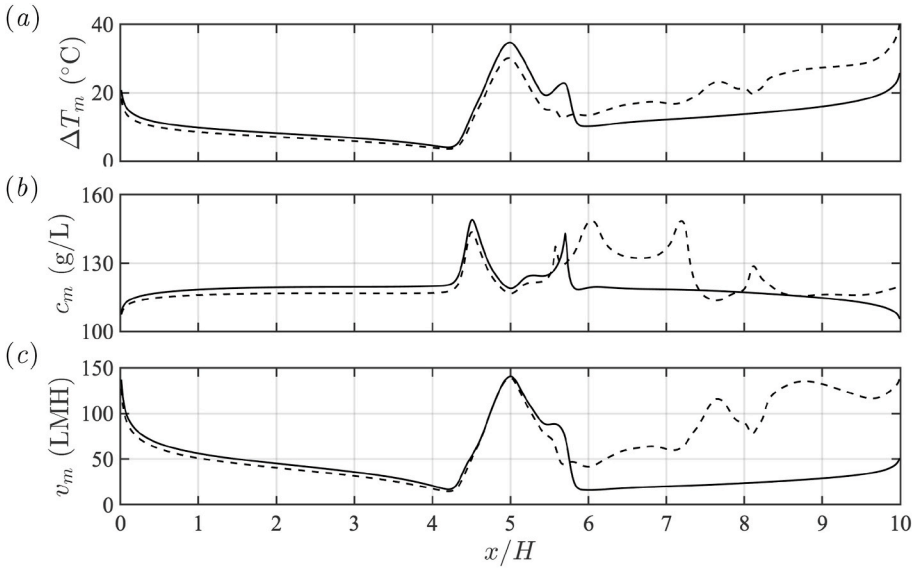

Fig. 29. Downstream variation of ΔT_m (*a*), c_m (*b*), and v_m (*c*) for $\widehat{y}_c = 0.3$ when $Re_f = 800$ (solid), 900 (dashed).

Fig. 29 shows the downstream variation of ΔT_m, c_m, and v_m for $\widehat{y}_c = 0.3$ when $Re_f = 800$ (solid) and 900 (dashed). Panel (*a*) shows that when $Re_f = 900$, membrane-vortices dramatically increase ΔT_m for $x/H > 6$. Panel (*b*) shows that membrane-vortices also produce multiple downstream regions of salt accumulation. Panel (*c*) shows that at $Re_f = 900$, v_m significantly increases for $x/H > 6$ due to increased ΔT_m.

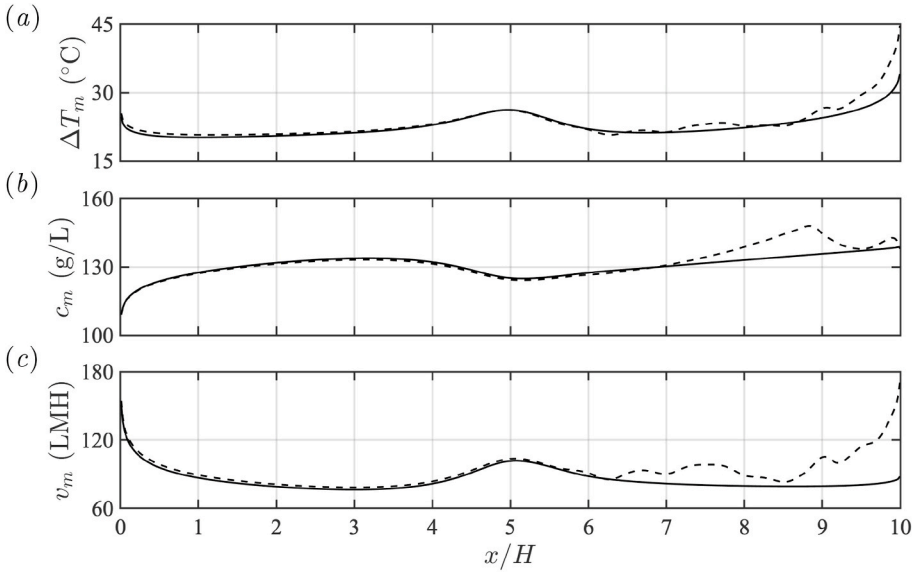

Fig. 30. Downstream variation of ΔT_m (*a*), c_m (*b*), and v_m (*c*) for $\widehat{y}_c = 0.7$ when $Re_f = 800$ (solid) and 900 (dashed).

Fig. 30 shows the downstream variation of ΔT_m (*a*), c_m (*b*), and v_m (*c*) for $\widehat{y}_c = 0.7$ when $Re_f = 800$ (solid) and 900 (dashed). We find that spacers placed near the outer plates decrease both temperature and concentration polarization in the steady regime. With the transition to vortex shedding, vapor production is further increased, but at the expense of increasing concentration polarization.

References

[1] K.L. Hickenbottom, T.Y. Cath, Comparative study of brine management technologies for desalination plants, J. Membr. Sci. 454 (2014) 426.
[2] R. Bouchrit, A. Boubakri, A. Hafiane, A.A.T. Bouguecha, Direct contact membrane distillation: capability to treat hyper-saline solution, Desalination 376 (2015) 117.
[3] A. Alkhudhiri, N. Darwish, N. Hilal, Membrane distillation: a comprehensive review, Desalination 287 (2012) 55.
[4] G. Chen, X. Yang, Y. Lu, R. Wang, A.G. Fane, Heat transfer intensification and scaling mitigation in bubbling-enhanced membrane distillation for brine concentration, J. Membr. Sci. 470 (2014) 60.
[5] G. Chen, Y. Lu, X. Yang, R. Wang, A. G. Fane, Quantitative study on crystallization-induced scaling in high-concentration direct-contact membrane distillation, Ind. Eng. Chem. Res. 53.
[6] C.M. Tun, A.G. Fane, J.T. Matheickal, R. Sheikholeslami, Membrane distillation crystallization of concentrated saltsflux and crystal formation, J. Membr. Sci. 257 (2005) 144.
[7] H.C. Duong, S. Gray, M. Duke, T.Y. Cath, L.D. Nghiem, Scaling control during membrane distillation of coal seam gas reverse osmosis brine, J. Membr. Sci. 493 (2015) 673.
[8] H.C. Duong, A.R. Chivas, B. Nelemans, M.D. adn, S. Gray, T.Y. Cath, L.D. Nghiem, Treatment of ro brine from csg produced water by spiral-wound air gap membrane distillationa pilot study, Desalination 366 (2015) 121.

[9] F. Edwie, T.S. Chung, Development of hollow fiber membranes for water and salt recovery from highly concentrated brine via direct contact membrane distillation and crystallization, J. Membr. Sci. 421422 (2012) 111–123.
[10] F. Edwie, T.S. Chung, Development of simultaneous membrane distillationcrystallization (smdc) technology for treatment of saturated brine, Chem. Eng. Sci. 98 (2013) 160–172.
[11] G. Guan, R. Wang, F. Wicaksana, X. Yang, A.G. Fane, Analysis of membrane distillation crystallization system for high salinity brine treatment with zero discharge using aspen flowsheet simulation, Ind. Eng. Chem. Res. 51 (2012) 1340513413.
[12] X. Ji, E.C.S.A. Obaidani, G.D. Profio, E. Fontananova, E. Drioli, Membrane distillation-crystallization of seawater reverse osmosis brines, Separ. Purif. Technol. 71 (2010) 76–82.
[13] L.M. Vane, Review: water recovery from brines and salt-saturated solutions: operability and thermodynamic efficiency considerations for desalination technologies, J. Chem. Technol. Biotechnol. 92 (10) (2017) 25062518.
[14] J. Lou, J. Vanneste, S.C. DeCaluwe, T.Y. Cath, N. Tilton, Computational fluid dynamics simulations of polarization phenomena in direct contact membrane distillation, J. Membr. Sci. 591 (2019) 117150.
[15] A. Matin, F. Rahman, H. Shafi, S. Zubair, Scaling of reverse osmosis membranes used in water desalination: phenomena, impact, and control; future directions, Desalination 455 (2019/04/01), 135 – 57.
[16] M. Xie, C.Y. Tang, S.R. Gray, Spacer-induced forward osmosis membrane integrity loss during gypsum scaling, Desalination 392 (2016) 85–90.
[17] P. Xu, C. Bellona, J.E. Drewes, Fouling of nanofiltration and reverse osmosis membranes during municipal wastewater reclamation: membrane autopsy results from pilot-scale investigations, J. Membr. Sci. 353 (1) (2010) 111–121.
[18] B.D. Coday, N. Almaraz, T.Y. Cath, Forward osmosis desalination of oil and gas wastewater: impacts of membrane selection and operating conditions on process performance, J. Membr. Sci. 488 (2015) 40–55.
[19] S. Lee, J. Kim, C.-H. Lee, Analysis of caso4 scale formation mechanism in various nanofiltration modules, J. Membr. Sci. 163 (1) (1999) 63–74.
[20] A.G. Pervov, Scale formation prognosis and cleaning procedure schedules in reverse osmosis systems operation, Desalination 83 (1) (1991) 77–118, proceedings of the Twelfth International Symposium on Desalination and Water Re-use.
[21] M.M. Gimmelshtein, R. Semiat, Investigation of flow next to membrane walls, J. Membr. Sci. 264 (1) (2005) 137–150.
[22] D.G. Thomas, P.H. Hayes, W.R. Mixon, J.D. Sheppard, W.L. Griffith, R.M. Keller, Turbulence promoters for hyperfiltration with dynamic membranes, Environ. Sci. Technol. 4 (12) (1970) 1129–1136.
[23] A. Subramani, S. Kim, E.M. Hoek, Pressure, flow, and concentration profiles in open and spacer-filled membrane channels, J. Membr. Sci. 277 (1) (2006) 7–17.
[24] D.G. von der Schulenburg], J. Vrouwenvelder, S. Creber, M. [van Loosdrecht], M. Johns, Nuclear magnetic resonance microscopy studies of membrane biofouling, J. Membr. Sci. 323 (1) (2008) 37–44.
[25] A. Haidari, S. Heijman, W. [van der Meer], Optimal design of spacers in reverse osmosis, Separ. Purif. Technol. 192 (2018) 441–456.
[26] S.M. Ali, A. Qamar, S. Kerdi, S. Phuntsho, J.S. Vrouwenvelder, N. Ghaffour, H. K. Shon, Energy efficient 3d printed column type feed spacer for membrane filtration, Water Res. 164 (2019) 114961.
[27] I.S. Ngene, R.G. Lammertink, M. Wessling, W.G.V. der Meer], Particle deposition and biofilm formation on microstructured membranes, J. Membr. Sci. 364 (1) (2010) 43–51.
[28] X. Xie, C.L. Men], N. Dietrich, P. Schmitz, L. Fillaudeau, Local hydrodynamic investigation by piv and cfd within a dynamic filtration unit under laminar flow, Separ. Purif. Technol. 198 (2018) 38–51, filtering a Better Future.
[29] A. Haidari, S. Heijman, W. [van der Meer], Visualization of hydraulic conditions inside the feed channel of reverse osmosis: a practical comparison of velocity between empty and spacer-filled channel, Water Res. 106 (2016) 232–241.
[30] O.R. Lokare, P. Ji, S. Wadekar, G. Dutt, R.D. Vidic, Concentration polarization in membrane distillation: I. development of a laser-based spectrophotometric method for in-situ characterization, J. Membr. Sci. 581 (2019) 462–471.
[31] H. Ahadi, J. Karimi-Sabet, M. Shariaty-Niassar, The effect of module geometry on heat and mass transfer in membrane distillation, Chem. Prod. Process Model. 11 (2016) 35–39.
[32] S. Al-Sharif, M. Albeirutty, A. Cipollina, G. Micale, Modelling flow and heat transfer in spacer-filled membrane distillation channels using open source cfd code, Desalination 311 (2013) 103–112.
[33] M. Bhattacharya, S.K. Dutta, J. Sikder, M.K. Mandal, Computational and experimental study of chromium (vi) removal in direct contact membrane distillation, J. Membr. Sci. 450 (2014) 447–456.
[34] C.H.H. Chang, J. Hsu, Analysis of heat transfer coefficients in direct contact membrane distillation modules using cfd simulation, J. Appl. Sci. Eng. 19 (2016) 197–206.
[35] H. Chang, J. Hsu, C. Chang, C. Ho, T. Cheng, Simulation study of transfer characteristics for spacer-filled membrane distillation desalination modules, Appl. Energy 185 (2017) 2045–2057.
[36] I. Janajreh, D. Suwwan, R. Hashaikeh, Assessment of direct contact membrane distillation under different configurations, velocities and membrane properties, Appl. Energy 185 (2017) 2058–2073.
[37] I. Janajreha, R.H.M.N. Hussaina, R. Ahmedb, Thermal efficiency enhancement of the direct contact membrane distillation: conductive layer integration and geometrical undulation, Appl. Energy 227 (2018 October 17) 7–17.
[38] A. Katsandri, A theoretical analysis of a spacer filled flat plate membrane distillation modules using cfd: Part i: velocity and shear stress analysis, Desalination 408 (2017) 145–165.
[39] A. Katsandri, A theoretical analysis of a spacer filled flat plate membrane distillation modules using cfd: Part ii: temperature polarisation analysis, Desalination 408 (2017) 166–180.
[40] I.J.B.S. Laliaa, R. Hashaikeh, A facile approach to fabricate superhydrophobic membranes with low contact angle hysteresis, J. Membr. Sci. 539 (2017) 144–151.
[41] M. Ghadiri, S. Fakhri, S. Shirazian, Modeling of water transport through nanopores of membranes in direct-contact membrane distillation process, Polym. Eng. Sci. 54 (2014) 660666.
[42] F.N. Ponzio, A. Tamburini, A. Cipollina, G. Micale, M. Ciofalo, Experimental and computational investigation of heat transfer in channels filled by woven spacers, Int. J. Heat Mass Tran. 104 (2017) 163–177.
[43] M. Shakaib, S. Hasani, I. Ahmed, R.M. Yunus, A cfd study on the effect of spacer orientation on temperature polarization in membrane distillation modules, Desalination 284 (2012) 332–340.
[44] Y. Taamneh, K. Bataineh, Improving the performance of direct contact membrane distillation utilizing spacer-filled channel, Desalination 408 (2017) 25–35.
[45] A. Cipollina, A.D. Miceli, J. Koschikowski, G. Micale, L. Rizzuti, Cfd simulation of a membrane distillation module channel, Desalin. Water Treat. 6 (2009) 177–183.
[46] A. Cipollina, G. Micale, L. Rizzuti, Membrane distillation heat transfer enhancement by cfd analysis of internal module geometry, Desalin. Water Treat. 25 (2011) 195–209.
[47] H. Yu, X. Yang, R. Wang, A.G. Fane, Numerical simulation of heat and mass transfer in direct membrane distillation in a hollow fiber module with laminar flow, J. Membr. Sci. 384 (2011) 107–116.
[48] H. Yu, X. Yang, R. Wang, A.G. Fane, Analysis of heat and mass transfer by cfd for performance enhancement in direct contact membrane distillation, J. Membr. Sci. 405–406 (2012) 38–47.
[49] X. Yang, H. Yu, R. Wang, A.G. Fane, Analysis of the effect of turbulence promoters in hollow fiber membrane distillation modules by computational fluid dynamic (cfd) simulations, J. Membr. Sci. 415–416 (2012) 758–769.
[50] X. Yang, H. Yu, R. Wang, A.G. Fane, Optimization of microstructured hollow fiber design for membrane distillation applications using cfd modeling, J. Membr. Sci. 421–422 (2012) 258–270.
[51] M.S. Salem, A.H. El-shazly, N. Nady, M.R. Elmarghany, M.A. Shouman, M. N. Sabry, 3-d numerical investigation on commercial ptfe membranes for membrane distillation: effect of inlet conditions on heat and mass transfer, Case Stud. Therm. Eng. 13 (2019) 100396.
[52] P. Yazgan-Birgi, M.I.H. Alia, H.A. Arafat, Comparative performance assessment of flat sheet and hollow fiber dcmd t processes using cfd modeling, Separ. Purif. Technol. 212 (2019) 709–722.
[53] F. Ahmeda, K. E. Kadia, R. Hashaikeha, I. Janajreha, Low energy membrane distillation: a numerical study on the role of conductive spacers, Int. Conf. Appl. Energy.
[54] H. Hayer, O. Bakhtiari, T. Mohammadi, Simulation of momentum, heat and mass transfer in direct contact membrane distillation: a computational fluid dynamics approach, J. Ind. Eng. Chem. 21 (2015) 1379–1382.
[55] N. Loussif, J. Orfi, Comparative study of air gap, direct contact and sweeping gas membrane distillation configurations, Membr. Water. Treat. 7 (2016) 71–86.
[56] J. Seo, Y.M. Kimb, J.H. Kim, Spacer optimization strategy for direct contact membrane distillation: shapes, configurations, diameters, and numbers of spacer filaments, Desalination 417 (2017) 9–18.
[57] M.W.N.S. Soukane, L. Francis, A. Alsaadic, N. Ghaffour, Effect of feed flow pattern on the distribution of permeate fluxes in desalination by direct contact membrane distillation, Desalination 418 (2017) 43–59.
[58] D.J. Park, E. Norouzi, C. Park, Experimentally-validated computational simulation of direct contact membrane distillation performance, Int. J. Heat Mass Tran. 129 (2019) 10311042.
[59] G. Fimbres-Weihs, D. Wiley, Review of 3d cfd modeling of flow and mass transfer in narrow spacer-filled channels in membrane modules, Chem. Eng. Process 49 (7) (2010) 759–781, process Intensification on Intensified Transport by Complex Geometries.
[60] I. Hitsov, T. Maere, K.D. Sitter, C. Dotremont, I. Nopens, Modelling approaches in membrane distillation: a critical review, Separ. Purif. Rev. 142 (2015) 48–64.
[61] M.M.A. Shirazi, A. Kargari, A.F. Ismail, T. Matsuura, Computational fluid dynamic (cfd) opportunities applied to the membrane distillation process: state-of-the-art and perspectives, Desalination 377 (2016) 73–90.
[62] A. Tamburini, M. Renda, A. Cipollina, G. Micale, M. Ciofalo, Investigation of heat transfer in spacer-filled channels by experiments and direct numerical simulations, Int. J. Heat Mass Tran. 93 (2016) 1190–1205.
[63] N. Tilton, E. Serre, D. Martinand, R.M. Lueptow, A 3d pseudospectral algorithm for fluid flows with permeable walls. application to filtration, Comput. Fluids 93 (2014) 129–145.
[64] V.A. Haaksman, A. Siddiqui, C. Schellenberg, J. Kidwell, J.S. Vrouwenvelder, C. Picioreanu, Characterization of feed channel spacer performance using geometries obtained by x-ray computed tomography, J. Membr. Sci. 522 (2017) 124–139.
[65] S.K. Karode, A. Kumar, Flow visualization through spacer filled channels by computational fluid dynamics i. - pressure drop and shear rate calculations for flat sheet geometry, J. Membr. Sci. 193 (1) (2001) 69–84.

[66] D. Dendukuri, S.K. Karode, A. Kumar, Flow visualization through spacer filled channels by computational fluid dynamics-ii: improved feed spacer designs, J. Membr. Sci. 249 (1) (2005) 41–49.
[67] R. Kodm, F. Vlask, D. nita, A. ernn, K. Bouzek, Spatially two-dimensional mathematical model of the flow hydrodynamics in a channel filled with a net-like spacer, J. Membr. Sci. 368 (1) (2011) 171–183.
[68] Y.-L. Li, K.-L. Tung, The effect of curvature of a spacer-filled channel on fluid flow in spiral-wound membrane modules, J. Membr. Sci. 319 (1) (2008) 286–297.
[69] Y.-L. Li, P.-J. Lin, K.-L. Tung, Cfd analysis of fluid flow through a spacer-filled disk-type membrane module, Desalination 283 (2011) 140–147, special issue in honour of Professor Tony Fane on his 70th Birthday.
[70] P. Sousa, A. Soares, E. Monteiro, A. Rouboa, A cfd study of the hydrodynamics in a desalination membrane filled with spacers, Desalination 349 (2014) 22–30.
[71] Z. Cao, D. Wiley, A. Fane, Cfd simulations of net-type turbulence promoters in a narrow channel, J. Membr. Sci. 185 (2) (2001) 157–176.
[72] V.V. Ranade, A. Kumar, Fluid dynamics of spacer filled rectangular and curvilinear channels, J. Membr. Sci. 271 (1) (2006) 1–15.
[73] J. Schwinge, D. Wiley, D. Fletcher, A cfd study of unsteady flow in narrow spacer-filled channels for spiral-wound membrane modules, Desalination 146 (1) (2002) 195–201.
[74] J. Schwinge, D.E. Wiley, D.F. Fletcher, Simulation of unsteady flow and vortex shedding for narrow spacer-filled channels, Ind. Eng. Chem. Res. 42 (20) (2003) 4962–4977.
[75] A. Alexiadis, D.E. Wiley, D.F. Fletcher, J. Bao, Laminar flow transitions in a 2d channel with circular spacers, Ind. Eng. Chem. Res. 46 (16) (2007) 5387–5396.
[76] C. Koutsou, S. Yiantsios, A. Karabelas, Direct numerical simulation of flow in spacer-filled channels: effect of spacer geometrical characteristics, J. Membr. Sci. 291 (1) (2007) 53–69.
[77] M. Shakaib, S. Hasani, M. Mahmood, Study on the effects of spacer geometry in membrane feed channels using three-dimensional computational flow modeling, J. Membr. Sci. 297 (1) (2007) 74–89.
[78] S.M. Mojab, A. Pollard, J.G. Pharoah, S.B. Beale, E.S. Hanff, Unsteady laminar to turbulent flow in a spacer-filled channel, Flow, Turbul. Combust. 92 (1) (2014) 563–577.
[79] J. Santos, V. Geraldes, S. Velizarov, J. Crespo, Investigation of flow patterns and mass transfer in membrane module channels filled with flow-aligned spacers using computational fluid dynamics (cfd), J. Membr. Sci. 305 (1) (2007) 103–117.
[80] M. Ciofalo, F. Ponzio, A. Tamburini, A. Cipollina, G. Micale, Unsteadiness and transition to turbulence in woven spacer filled channels for membrane distillation, J. Phys. Conf. 796 (2017), 012003.
[81] F. Li, W. Meindersma, A. de Haan, T. Reith, Optimization of commercial net spacers in spiral wound membrane modules, J. Membr. Sci. 208 (1) (2002) 289–302.
[82] F. Li, W. Meindersma, A. de Haan, T. Reith, Experimental validation of cfd mass transfer simulations in flat channels with non-woven net spacers, J. Membr. Sci. 232 (1) (2004) 19–30.
[83] F. Li, W. Meindersma, A. de Haan, T. Reith, Novel spacers for mass transfer enhancement in membrane separations, J. Membr. Sci. 253 (1) (2005) 1–12.
[84] A. Ahmad, K. Lau, Impact of different spacer filaments geometries on 2d unsteady hydrodynamics and concentration polarization in spiral wound membrane channel, J. Membr. Sci. 286 (1) (2006) 77–92.
[85] G.A. Fimbres-Weihs, D.E. Wiley, D.F. Fletcher, Unsteady flows with mass transfer in narrow zigzag spacer-filled channels: a numerical study, Ind. Eng. Chem. Res. 45 (19) (2006) 6594–6603.
[86] K. Lau, M.A. Bakar, A. Ahmad, T. Murugesan, Feed spacer mesh angle: 3d modeling, simulation and optimization based on unsteady hydrodynamic in spiral wound membrane channel, J. Membr. Sci. 343 (1) (2009) 16–33.
[87] K.K. Lau, M.Z. Abu Bakar, A.L. Ahmad, T. Murugesan, Effect of feed spacer mesh length ratio on unsteady hydrodynamics in 2d spiral wound membrane (swm) channel, Ind. Eng. Chem. Res. 49 (12) (2010) 5834–5845.
[88] Y. Matsumura, T.L. Jackson, Numerical simulation of fluid flow through random packs of cylinders using immersed boundary method, Phys. Fluids 26 (4) (2014), 043602.
[89] D.L. Koch, A.J.C. Ladd, Moderate Reynolds number flows through periodic and random arrays of aligned cylinders, J. Fluid Mech. 349 (1997) 3166.
[90] R. Mittal, G. Iaccarino, Immersed boundary methods, Annu. Rev. Fluid Mech. 37 (1) (2005) 239–261.
[91] J. Lou, J. Johnston, N. Tilton, Application of projection and immersed boundary methods to simulating heat and mass transport in membrane distillation, Comput. Fluids 212 (2020) 104711.
[92] C.H.K. Williamson, Vortex dynamics in the cylinder wake, Annu. Rev. Fluid Mech. 28 (1) (1996) 477–539.
[93] V. Geraldes, V. SemiÂ£o, M.N. [de Pinho], The effect of the ladder-type spacers configuration in nf spiral-wound modules on the concentration boundary layers disruption, Desalination 146 (1) (2002) 187–194.
[94] V. Geraldes, V. SemiÂ£o, M.N. [de Pinho], Flow management in nanofiltration spiral wound modules with ladder-type spacers, J. Membr. Sci. 203 (1) (2002) 87–102.
[95] K.W. Lawson, D.R. Lloyd, Membrane distillation, J. Membr. Sci. 124 (1997) 1–25.
[96] R.W. Schofield, A.G. Fane, C.J.D. Fell, Heat and mass transfer in membrane distillation, J. Membr. Sci. 33 (1987) 299–313.
[97] J.M. Smith, H.C.V. Ness, Introduction to Chemical Engineering Thermodynamics, McGraw-Hill, 1975.
[98] L.G. Leal, Advanced Transport Phenomena: Fluid Mechanics and Convective Transport Processes, Cambridge University Press, 2007.
[99] R.B. Bird, W.E. Stewart, E.N. Lightfoot, Transport Phenomena, John Wiley & Sons, 2007.
[100] M. Sahin, R.G. Owens, A numerical investigation of wall effects up to high blockage ratios on two-dimensional flow past a confined circular cylinder, Phys. Fluids 16 (5) (2004) 1305–1320.
[101] J. Vanneste, J.A. Bush, K.L. Hickenbottom, C.A. Marks, D. Jassby, C.S. Turchid, T. Y. Cath, Novel thermal efficiency-based model for determination of thermal conductivity of membrane distillation membranes, J. Membr. Sci. 548 (2018) 298–308.
[102] M. Khayet, Membranes and theoretical modeling of membrane distillation: a review, Adv. Colloid Interface Sci. 164 (2011) 56–88.
[103] F. Lagan, G. Barbieri, E. Drioli, Direct contact membrane distillation: modelling and concentration experiments, J. Membr. Sci. 166 (1) (2000) 1–11.
[104] A. Lio, N. Lior, Critical review of membrane distillation performance criteria, Desalin. Water Treat. 56 (2016) 2009320140.